

Radiation pressure confinement – V. The predicted free-free absorption and emission in active galactic nuclei

Alexei Baskin¹★ and Ari Laor²★

¹*Plasma Physics Department, Soreq Nuclear Research Center, Yavne 8180000, Israel*

²*Physics Department, Technion – Israel Institute of Technology, Haifa 3200000, Israel*

Accepted 2021 September 7. Received 2021 August 21; in original form 2021 April 13

ABSTRACT

The effect of radiation pressure compression (RPC) on ionized gas in Active Galactic Nuclei (AGN) likely sets the photoionized gas density structure. The photoionized gas free-free absorption and emission are therefore uniquely set by the incident ionizing flux. We use the photoionization code Cloudy RPC model results to derive the expected relations between the free-free emission and absorption properties and the distance from the AGN centre, for a given AGN luminosity. The free-free absorption frequency of RPC gas is predicted to increase from ~ 100 MHz on the kpc scale, to ~ 100 GHz on the sub-pc scale, consistent with observations of spatially resolved free-free absorption. The free-free emission at 5 GHz is predicted to yield a radio loudness of $R \sim 0.03$, below the typical observed values of $R \sim 0.1 - 1$ in radio-quiet AGN. However, the flat free-free radio continuum may become dominant above 100 GHz. The suggested detection of optically thin free-free emission in NGC 1068, on the sub pc torus scale, is excluded as the brightness temperature is too high for optically thin free-free emission. However, excess emission observed with ALMA above 150 GHz in NGC 1068, is consistent with the predicted free-free emission from gas just outside the broad line region, a region which overlaps the hot dust disc resolved with GRAVITY. Extended ~ 100 pc scale free-free emission is also likely present in NGC 1068. Future sub mm observation of radio quiet AGN with ALMA may allow to image the free-free emission of warm photoionized gas in AGN down to the 30 mas scale, including highly absorbed AGN.

Key words: galaxies: active – quasars: general – radio continuum: galaxies

1 INTRODUCTION

Free-free absorption of radio emission is observed in some AGN (e.g. O’Dea & Saikia 2021), and is sometimes spatially resolved, allowing to map the distribution of the absorbing gas density and column density (Vermeulen et al. 1994; Walker et al. 1994; Levinson et al. 1995; Ulvestad et al. 1999; Ulvestad 1999; Gallimore et al. 1999; Pedlar et al. 1998; Walker et al. 2000; Jones et al. 2001; Middelberg et al. 2004). Free-free radio emission is expected from photoionized gas in AGN (Ulvestad et al. 1981; Krolik & Lepp 1989), and is possibly detected in some AGN (Antonucci & Barvainis 1988; Barvainis et al. 1996; Mundell et al. 2000; Gallimore et al. 2004; Carilli et al. 2019). The density and ionization structure of photoionized gas in AGN are likely set by the incident ionizing radiation energy and momentum fluxes (see below), and one can therefore derive the expected free-free absorption and emission of the gas just from its distance from the AGN centre. The purpose of this study is to provide detailed predictions of these properties, which can provide new constraints on photoionized gas in AGN, using the high angular resolution of the mm arrays, and the great penetration power of the mm radiation. Below, we briefly review the Radiation Pressure Compression (RPC) mechanism, which sets both the gas density structure and the gas ionization structure.

Radiation deposits both energy and momentum when it interacts with gas. The energy deposition and the resulting gas emission received much attention, and is calculated by highly detailed photoionization modelings (e.g. Ferland et al. 2017). The radiation momentum deposition, specifically the radiation force per unit mass, is commonly considered significant if it becomes comparable to gravity. This is relevant from the stellar structure scale (Eddington 1916), out to the galaxy structure scale (e.g. Thompson et al. 2005; Murray et al. 2010). Radiative acceleration can dominate the gas dynamics, and whether the system remains gravitationally bound. However, another critical parameter is the ratio of the radiation pressure to the other internal forces in the gas, in particular the gas pressure. If the gas is in free fall, say in a Keplerian orbit, then gravity is zero in the gas frame, and the only remaining net forces (in the absence of significant magnetic fields) are the radiation flux gradient and the gas pressure gradient within the gas.

The energy deposition of the incident ionizing radiation and the gas cooling set the gas equilibrium temperature. The gas density in photoionization modelings is often considered a free parameter. However, if the gas pressure gradient is lower than the opposing incident radiation pressure gradient, then radiation pressure inevitably compresses the gas. This compression builds up the gas pressure, until a local equilibrium is achieved. The built up gas pressure at the depth where the incident radiation is fully absorbed, matches then the incident radiation pressure. Thus, the gas density is not a free param-

★ E-mail: alexeiba@soreq.gov.il (AB); laor@physics.technion.ac.il (AL)

ter, as the gas pressure, and also its temperature, are set by the incident radiation pressure. This RPC effect implies that the gas temperature structure and the density structure are both set by the incident radiation. The RPC effect was described in a few studies (Pier & Voit 1995; Binette 1998; Dopita et al. 2002; Draine 2011b), in the context of gas in the Narrow Line Region (NLR) in AGN and gas in H II regions. The RPC effect has profound implications on the emission and absorption line properties of gas in AGN. It likely produces the observed density distance relation of $n \propto r^{-2}$ in the NLR (Stern, Laor & Baskin 2014a), the relative strength and the radial dependence of the lines from the Broad Line Region (BLR; Baskin, Laor & Stern 2014a). It also explains the universal absorption measure distribution observed in AGN over a wide range of ionization states (Stern et al. 2014b), and why the fast outflows in broad absorption line quasars are not overionized (Baskin, Laor & Stern 2014b). The RPC effect also produces the observed universal differential emission measure of the X-ray narrow lines in AGN (Bianchi et al. 2019).

The photoionized gas cools by line and continuum emission, in particular free-free emission. The purpose of this study is to use the RPC modelings to find the expected radio free-free absorption and emission signature of RPC gas in AGN. As we show below, the free-free absorption optical depth provides the distance of the absorbing gas from the centre. The radio free-free emission may be the dominant emission mechanism in radio quiet AGN in the mm range. The unique advantage of the mm emission is that it is effectively unabsorbable. It can penetrate any column of neutral gas, and also the expected ionized column of photoionized gas. The sensitivity of current mm arrays may allow to image the free-free emission sources, and thus image photoionized gas, also in highly absorbed AGN, on scales of ~ 100 mas and below, which is not achievable in other bands.

The paper is organized as follows. In Section 2 we describe the free-free emission from RPC photoionized gas, and provide analytic approximations. In Section 3 we provide the results for a variety of possible configurations. The results are compared with observations in Section 4 and discussed in Section 5. In Section 6 we provide the main conclusions.

2 THE MODEL

2.1 Simplified estimates

We show below that RPC implies a nearly constant ratio of free-free luminosity density to bolometric luminosity, L_ν/L_{bol} , in AGN. This ratio depends only on whether the line emitting gas is dusty (NLR), or dustless (BLR), and on the gas covering factor Ω (the fraction of 4π covered). The relation holds for optically thin emission, a condition which can be verified from the observed spectral slope (see below).

The free-free emissivity is

$$\epsilon_\nu = \frac{2^5 \pi e^6}{3m_e c^3} \left(\frac{2\pi}{3km_e} \right)^{1/2} T^{-1/2} Z_i^2 n_e n_i e^{-h\nu/kT} \bar{g}_{\text{ff}}, \quad (1)$$

where n_e and n_i are the electron and ion number density, for ions of charge Z_i , T is the gas temperature, and \bar{g}_{ff} is the velocity averaged Gaunt factor (e.g. Rybicki & Lightman 2004, eq. 5.14a). Most of the ionizing continuum is absorbed near the H ionization front where $T \sim 10^4$ K. In the radio $h\nu \ll kT$, and thus $e^{-h\nu/kT} \approx 1$. The velocity averaged Gaunt factor is $\bar{g}_{\text{ff}} \approx 4$ (Draine 2011a). In the analytic estimates below, we assume for simplicity H-only gas (i.e. $Z_i = 1$). The approximations above yield an emissivity of

$$\epsilon_\nu \approx 2.7 \times 10^{-39} n_e n_i \text{ erg s}^{-1} \text{ Hz}^{-1} \text{ cm}^{-3}. \quad (2)$$

The RPC effect predicts that the ionized gas is compressed to a density of

$$n \approx 1.8 L_{\text{bol}} r^{-2} \text{ cm}^{-3}, \quad (3)$$

near the H ionization front (Stern et al. 2014a, eq. 6), with a compression length-scale of (Baskin et al. 2014a, eq. 14)

$$l = \frac{2kTc}{\bar{\sigma}} \left(\frac{L_{\text{bol}}}{4\pi r^2} \right)^{-1} = 1\bar{\sigma}^{-1} L_{\text{bol}}^{-1} r^2 \text{ cm}, \quad (4)$$

where $\bar{\sigma} \approx 10^{-21} \text{ cm}^{-2}$ for dusty gas, and $\bar{\sigma} \approx 10^{-22} \text{ cm}^{-2}$ for dustless ionized gas at the highest density near the ionization front. Note that L_{bol} and r are in cgs units. Equation 4 implies that l is typically small compared to r with

$$\frac{l}{r} = 3 \times 10^{-7} \sigma_{-21}^{-1} L_{46}^{-1} r_{\text{pc}}, \quad (5)$$

where $\bar{\sigma} \approx 10^{-21} \sigma_{-21}$, $L_{\text{bol}} = 10^{46} L_{46}$ and $r = 1 r_{\text{pc}}$ pc. Thus, the specific free-free luminosity from a photoionized uniform density slab, of thickness l , distance r from the centre, with a solid angle $4\pi\Omega$, is approximately

$$L_\nu = 4\pi r^2 \Omega l \epsilon_\nu \approx 1 \times 10^{-37} \Omega \bar{\sigma}^{-1} L_{\text{bol}} \text{ erg s}^{-1} \text{ Hz}^{-1}, \quad (6)$$

which implies

$$L_\nu/L_{\text{bol}} \approx \begin{cases} 10^{-16} \Omega \text{ Hz}^{-1} & \text{for dusty gas,} \\ 10^{-15} \Omega \text{ Hz}^{-1} & \text{for dustless gas.} \end{cases} \quad (7)$$

The fraction of bolometric luminosity converted to free-free emission, L_ν/L_{bol} , depends only on Ω , the covering factor of the reprocessing gas. The proportionality of $L_\nu \propto L_{\text{bol}}$ is a general property of photoionized gas, but the exact quantitative relation depends on the gas density, which sets the gas temperature and ionization state. The new result of RPC is that the proportionality coefficient is uniform in a given AGN, and among all AGN, as the ionization structure in the illuminated gas is universal.

The threshold value, ν_{thick} , below which the gas becomes optically thick to free-free absorption can be evaluated as follows. The free-free absorption coefficient is (e.g. Rybicki & Lightman 2004, eq. 5.18a)

$$\alpha_\nu = \frac{4e^6}{3m_e hc} \left(\frac{2\pi}{3km_e} \right)^{1/2} T^{-1/2} Z_i^2 n_e n_i \nu^{-3} \left(1 - e^{-h\nu/kT} \right) \bar{g}_{\text{ff}}. \quad (8)$$

In the radio, $h\nu \ll kT$ and thus

$$\alpha_\nu \approx 0.08 T^{-3/2} n_e n_i \nu^{-2} \text{ cm}^{-1}, \quad (9)$$

for $Z_i = 1$ and $\bar{g}_{\text{ff}} \approx 4$. The slab is optically thick when $\tau_\nu = \alpha_\nu l > 1$, where l is given by eq. 4, which for $T = 10^4$ K occurs below the frequency

$$\nu_{\text{thick}} = \sqrt{8 \times 10^{-8} \bar{\sigma}^{-1} L_{\text{bol}} r^{-2}}. \quad (10)$$

It is convenient to define the quantity

$$r_{\text{dust}} \equiv 0.2 L_{46}^{0.5} \text{ pc}, \quad (11)$$

which is roughly the sublimation radius of large graphite grain (see Baskin & Laor 2018). Since, $L_{\text{bol}} = 2.63 \times 10^{10} r_{\text{dust}}^2$ in cgs, we get

$$\nu_{\text{thick}} = \begin{cases} 1.5 \times 10^{12} (r/r_{\text{dust}})^{-1} \text{ Hz} & \text{for dusty gas,} \\ 4.6 \times 10^{12} (r/r_{\text{dust}})^{-1} \text{ Hz} & \text{for dustless gas.} \end{cases} \quad (12)$$

The free-free emission becomes self-absorbed at $\nu < \nu_{\text{thick}}$, and if the gas is isothermal, the emission approaches a blackbody ($L_\nu \propto \nu^2$), in contrast with the flat optically thin spectrum ($L_\nu \propto \nu^{-0.1}$) at $\nu > \nu_{\text{thick}}$.

One should note that the radio emission cannot propagate freely in plasma below the plasma frequency,

$$\nu_p = \sqrt{\frac{ne^2}{\pi m_e}} \approx 1.6 \times 10^4 L_{\text{bol}}^{1/2} r^{-1} \text{ Hz}, \quad (13)$$

where n is taken from eq. 3. Equivalently,

$$\nu_p \approx 2.6 \times 10^9 (r/r_{\text{dust}})^{-1} \text{ Hz}, \quad (14)$$

which is lower than the above estimates of ν_{thick} by a factor of $\sim 10^3$. The gas is highly optically thick at ν_p , and its emission approaches a blackbody ($L_\nu \propto \nu^2$) already at ν_{thick} . Thus, L_ν drops by a factor of 10^6 from ν_{thick} to ν_p , and the free-free contribution is negligible already above the frequency where the plasma cutoff sets in.

The above estimate of L_ν/L_{bol} (eq. 7) applies for optically thin free-free emission, i.e. at $\nu > \nu_{\text{thick}}$. Below we derive the free-free emission based on a numerical photoionization solution which includes RPC. We use the equation of \bar{g}_{ff} from [Draine \(2011a, section 10.2\)](#). For convenience we set $\epsilon_\nu = 0$ for $\nu < 10\nu_p$.

2.2 The numerical solution

Below we evaluate the structure of a photoionized RPC gas slab, i.e. the solution for n_e , n_i and T , as a function of depth into the slab. We follow the procedure detailed in [Baskin et al. \(2014a\)](#). The structure is calculated using the photoionization code Cloudy 13.03 ([Ferland et al. 2013](#)). An open geometry is assumed. We use the Cloudy command ‘constant pressure’ to set the total pressure constant throughout the calculation. We also utilize the command ‘no radiation pressure’ to exclude the radiation pressure due to trapped line emission, as otherwise the Cloudy solution scheme may become unstable ([Baskin et al. 2014a](#)). We assume gas metallicity of $Z = 2Z_\odot$, and use the scaling law of metals with Z from [Groves et al. \(2004\)](#). The intermediate ionizing spectral slope of $\alpha_{\text{ion}} = -1.6$ is adopted from [Baskin et al. \(2014a\)](#), with $f_\nu \propto \nu^{\alpha_{\text{ion}}}$ between 1 Ryd and 1 keV (912–12 Å). The calculation is stopped when the H ionized fraction (H^+/H) drops to 1 per cent. The solution of an RPC slab is independent of the initial density n_0 at the illuminated face of the slab, if $P_{\text{rad}} \gg P_{\text{gas}}$ at the illuminated face ([Stern et al. 2014a; Baskin et al. 2014a](#)). For the BLR calculations, specifically for regions at $0.1 < r/r_{\text{dust}} \leq 1$, we set $n_0 = 10^4 \text{ cm}^{-3}$. For regions further inwards at $r/r_{\text{dust}} \leq 0.1$, we set $n_0 = 10^6 \text{ cm}^{-3}$. For regions outside the BLR we use $n_0 = 100 \text{ cm}^{-3}$, except for dustless calculations at $1 < r/r_{\text{dust}} \leq 10$ which are set with $n_0 = 10^4 \text{ cm}^{-3}$. For region at $r/r_{\text{dust}} > 10^4$ we use $n_0 = 1 \text{ cm}^{-3}$. These values for n_0 ensure that $P_{\text{rad}} \gg P_{\text{gas}}$ holds at the illuminated face, and that the slab total width is significantly smaller compared to r (by a factor of ≥ 10).

The structure of an RPC slab is set by the incident flux, i.e. by the value of L_{bol}/r^2 , rather than by L_{bol} and r independently. We therefore construct a grid of models for $L_{46} = 1$, varying only r . Finally, we assume that the gas is either dustless or dusty. For the dusty-gas models, we assume the Galactic ISM grain composition and metal depletion, and a linear scaling of the dust-to-gas ratio with Z .

The free-free emission spectrum is calculated by using the evaluated structure of the photoionized slab. A Cloudy calculation results in a solution of the slab which is divided into consecutive ‘zones’. Each zone is defined by its width Δr_z and distance from the continuum source r_z . Cloudy solves for the physical parameters n_e , n_i and T in each zone. We use these parameters to calculate ϵ_ν and α_ν (eqs. 1 and 8, respectively) of each zone. We sum over the contribution of the most abundant elements: H, He, C, N, O and Ne, i.e. those

which satisfy $X/\text{H} > 10^{-4}$ for $Z = 2Z_\odot$ (for $Z = Z_\odot$, we adopt the solar composition set in Cloudy). We evaluate \bar{g}_{ff} in eqs. 1 and 8 by adopting the two following relations from [Draine \(2011a\)](#)

$$\bar{g}_{\text{ff}}(\nu) = \frac{\sqrt{3}}{\pi} \left[\ln \frac{(2kT)^{3/2}}{\pi Z_i e^2 m_e^{1/2} \nu} - \frac{5\gamma}{2} \right], \quad (15)$$

for $h\nu \leq kT/10^3$, where $\gamma = 0.577$ is Euler’s constant; and

$$\bar{g}_{\text{ff}}(\nu) = \ln \left\{ \exp \left[5.960 - \frac{\sqrt{3}}{\pi} \ln \left(Z_i \frac{\nu}{10^9} \left(\frac{T}{10^4} \right)^{-3/2} \right) \right] + e \right\}, \quad (16)$$

otherwise. The difference between the two relations near the transition ν , i.e. at $h\nu \approx kT/10^3$, is smaller than 5 per cent. Near the H ionization front, where $T \approx 10^4$ K, both relations imply $\bar{g}_{\text{ff}}(\nu) \sim \nu^{-0.10}$ for $\nu \approx 1 - 10$ GHz. The power-law slope steepens slightly for larger values of ν ; and at $\nu \approx 100$ GHz, the slope equals -0.16 and -0.14 for eqs. 15 and 16, respectively.

The specific luminosity produced by a given zone of width Δr_z inside the slab is

$$L_{\nu,z}^{\text{em}} = 4\pi\Omega r_z^2 \Delta r_z \epsilon_\nu. \quad (17)$$

We account for the effect of free-free absorption by the emitting zone itself by taking the luminosity that is emitted by the zone toward the two neighbouring zones as

$$L_{\nu,z} = L_{\nu,z}^{\text{em}} \exp(-\alpha_\nu \Delta r_z/2). \quad (18)$$

The specific luminosity of a particular zone that escapes the slab from a given side (either the illuminated or back side) is evaluated as

$$L_{\nu,z}^{\text{esc}} = L_{\nu,z} \exp \left(- \sum_i \alpha_{\nu,i} \Delta r_{z,i} \right), \quad (19)$$

where the summation is over all zones that are located between the particular zone and the front or back surface. The total emitted spectrum from a given side, which we present below, equals

$$L_\nu = \sum_z L_{\nu,z}^{\text{esc}}, \quad (20)$$

where the summation is over all zones.

For the sake of comparison, we also calculate the free-free emission from the commonly used uniform gas density photoionization models. The Cloudy calculations are executed in a similar setting to the RPC calculation, as described above. The main differences are the following. First, the gas density n , rather than the total P , is kept constant at the assumed value. Second, the density of ionizing photons at the illuminated side of the slab, n_γ , is set by n and the ionization parameter $U \equiv n_\gamma/n$, rather than by r/r_{dust} . Finally, the stopping criterion is either reaching a H ionization fraction of 1 per cent, as for the RPC calculations, or a total H column of $\Sigma_{\text{H}} = 5 \times 10^{24} \text{ cm}^{-2}$ (RPC solutions always reach the criterion of ionization fraction prior to reaching this Σ_{H}). Only the highest $\log U = 1$ dustless calculation stops due to the Σ_{H} criterion (reaching a H ionization fraction of ~ 1.5 per cent at the back side). All other dustless calculations terminate at the 1 per cent H ionization fraction; and all dusty calculations stop because they reach the default Cloudy lower limit on the temperature of $T = 4000$ K. The procedure for evaluating the outgoing free-free emission is the same as described above for the RPC models.

3 RESULTS

3.1 The gas density and temperature structure

The common approach when calculating free-free absorption and emission is to assume a uniform density and temperature structure (e.g. Ulvestad et al. 1981; Krolik & Lepp 1989). However, as discussed above, the observations suggest that the gas density distribution in the NLR and the BLR in AGN is set by the incident radiation pressure (e.g. Stern et al. 2014a; Baskin et al. 2014a). Below we describe the density and temperature structure induced by RPC in a given gas cloud, and the resulting free-free emission distribution within the cloud.

Figure 1 (upper panels) presents the temperature and the electron density structure as a function of depth d in the slab, where d is measured from the back side where the H ionization fraction drops to 1 per cent (see Section 2.2). We use d rather than the depth from the illuminated face of the slab, since the RPC structure solution is independent of the boundary condition at the illuminated face, when plotted as a function of d , i.e. the depth from a layer where the ionization fraction drops to a given value (chosen here as 0.01; e.g. Baskin et al. 2014a, fig. 2). The structure is presented for dusty and dustless gas situated at $r/r_{\text{dust}} = 10$. In both cases, the temperature decreases from $T \gtrsim 10^6$ K near the illuminated side of the slab (the Compton temperature; see Baskin et al. 2014a) to $T \approx 10^4$ K at the H ionization front. Beyond the ionization front the gas becomes partly neutral, and $T \lesssim 10^4$ K. The electron density increases from its assumed initial value at the illuminated side ($\log n_{e,0} = 2$ and 4 for the dusty and dustless model, respectively; Section 2.2), to $\log n_e \approx 8$ reached at the H ionization front for both models. Inward of the H ionization front, n_e decreases as the gas becomes only partly ionized. The maximal n_e is similar in both models, as it is set by the incident radiation pressure, which is identical for both (eq. 3). In the dusty gas, the increase in n_e with decreasing d is smooth (Fig. 1, top-left panel), as the increase in the gas pressure is set by the absorbed radiative flux, absorption set by the dust opacity which is independent of the gas T and n . For the dustless gas, the density structure is set by the gas opacity, which depends critically on the local T and n , leading to sharp changes in the density with d (Fig. 1, top-right panel). The compression length scale near the ionization front is ~ 1 dex smaller for the dusty model since $\sigma_{-21} = 1$ for dusty gas, while $\sigma_{-21} = 0.1$ for dustless gas near the ionization front, where $U \sim 0.1$ (see also eq. 4). The dustless gas compression length scale increases towards the face of the slab, as U increases until the gas is fully ionized, with only Thomson cross section $\sigma_{-21} = 6.65 \times 10^{-4}$. As a result, the total thickness of the dustless slab is larger by ~ 2 dex than for a dusty slab.

Figure 1 (lower panels) presents the free-free luminosity that originates at a given d and emerges from the illuminated face of the slab, at several values of ν . For the purpose of clarity, we plot the luminosity per logarithmic unit depth, since the depth extends over 3–4 orders of magnitude. The emitted luminosity is corrected for the free-free absorption between the emission point d and the illuminated face (eq. 19). The calculation assumes $\Omega = 0.3$ and $L_{46} = 1$ (the free-free luminosity scales linearly with Ω and L_{bol}). The local emission follows the density structure since $\epsilon_\nu \sim n_e^2$ (eq. 2), as long as the layer is optically thin. Since $\alpha_\nu \sim n_e^2 T^{-3/2} \nu^{-2}$ (eq. 9), there is a sharp increase in τ_ν inwards as n_e increases and T decreases. Once $\tau_\nu > 1$ the emission becomes self-absorbed, leading to a cutoff in the outgoing emission with decreasing d (Fig. 1, bottom panels). With increasing ν the depth (from the illuminated side) where $\tau_\nu > 1$ increases. At a large enough ν , the whole photoionized layer becomes optically thin, i.e. $\tau_\nu < 1$ everywhere, leading to optically thin free-

free emission at that ν . The contribution to the free-free emission from the partly neutral gas beyond the ionization front decreases due to the decreasing n_e . Most of the emission in the optically thin case, originates from gas close to the ionization front. In the optically thick case, most of the free-free emission originates at the $\tau_\nu \sim 1$ layer.

3.2 Free-free absorption

Figure 2 presents the free-free absorption of radiation transmitted through a photoionized RPC gas slab. The slab is located at various distances from the photoionizing source, and is either dusty or dustless. Since the free-free absorption coefficient $\alpha_\nu \propto \nu^{-2}$ (eq. 9) all slabs become optically thick below a certain frequency, ν_{thick} . Dustless gas has a higher ν_{thick} than dusty gas at a given location (see Fig. 2). The dustless gas has a larger ν_{thick} , as the ionized layer extends deeper, i.e. larger l , due to the lower value of $\bar{\sigma}$ (Section 2), which produces a larger $\tau_\nu = \alpha_\nu l$.

Photoionized gas close to the BLR is highly absorptive in the radio, up to the mm regime, and becomes transparent only in the sub mm for dusty gas ($\nu > 300$ GHz, $\lambda < 1$ mm), and only in the FIR for dustless gas ($\nu > 3$ THz, $\lambda < 100 \mu\text{m}$). In contrast, photoionized gas at the NLR ($r/r_{\text{dust}} > 10^3$) becomes transparent already at ~ 1 GHz.

The simple analytic estimate made above (eq. 12) gives $\nu_{\text{thick}} \propto r^{-1}$. The best fit relation for $\nu_{\text{thick}}(r)$, using the Cloudy RPC model solutions (Fig. 2), yields

$$\nu_{\text{thick}} = \begin{cases} 6.03 \times 10^{11} (r/r_{\text{dust}})^{-0.95} \text{ Hz} & \text{for dusty gas,} \\ 5.01 \times 10^{12} (r/r_{\text{dust}})^{-1.42} \text{ Hz} & \text{for dustless gas,} \end{cases} \quad (21)$$

based on dusty gas solutions at $1 \leq r/r_{\text{dust}} \leq 10^4$, and dustless gas solutions at $0.3 \leq r/r_{\text{dust}} \leq 10$.

The clear spectral signature of free-free absorption is through the presence of a sharp cutoff in the observed spectrum below a given frequency, which follows $\tau_\nu \propto \nu^{-2}$ (eq. 9). The value of ν_{thick} allows to measure directly the distance of the free-free absorbing screen from the ionizing source.

Free-free absorption of a background radio source can be produced by any foreground ionized gas source. The absorbing gas can be heated by other processes, such as shocks, and not necessarily photoionization. If the distance of the absorbing medium from the central source is known through other observations, then eq. 21 can be used to test if the absorbing gas is heated by photoionization, and if its density structure is set by RPC.

If the radio source happens to be free-free emission of photoionized gas, then the source free-free emission is always expected to become self-absorbed below ν_{thick} , even in the absence of a foreground screen, as further discussed below.

3.3 Free-free emission

3.3.1 Emission from the illuminated side

Figure 3 presents the emitted spectrum from the illuminated face of a gas slab (eq. 20), located at various values of r/r_{dust} . The relative strength of the free-free luminosity, L_ν/L_{bol} , is set by the covering factor of the slab that is assumed here $\Omega = 0.3$, which is typical for the BLR (e.g. Baskin et al. 2014a). At a given distance, the emission at $\nu > \nu_{\text{thick}}$ is optically thin, with $L_\nu \propto \nu^{-0.1}$, and steepens slightly to $L_\nu \propto \nu^{-0.2}$ above 100 GHz (due to the change in the frequency dependence of \bar{g}_{ff}). The emission becomes optically thick at $\nu < \nu_{\text{thick}}$, and for an isothermal gas the free-free emission becomes a blackbody, which at the Rayleigh-Jeans regime gives

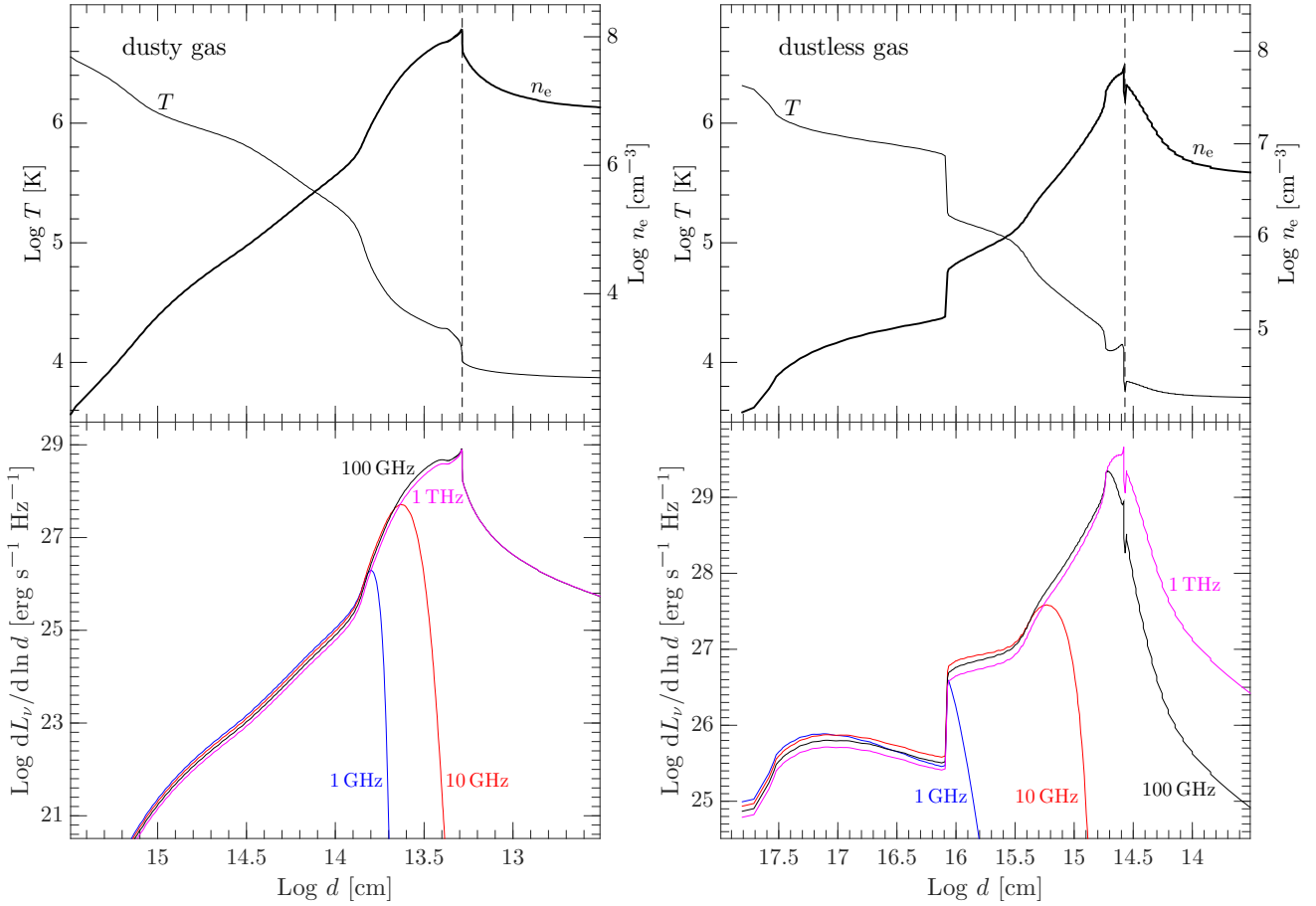


Figure 1. Upper panels: The electron density and temperature structure of an RPC dusty (left) or dustless (right) slab located at $r = 10r_{\text{dust}}$. The position of the ionization front (where $n_e = 0.5n$) is marked (dashed vertical line). The value of T drops from the Compton value close to the face of the slab, to $T \approx 10^4$ K at the H ionization front. The value of n_e increases sharply from the low boundary values to the ionization front, where $n_e \approx 10^8 \text{ cm}^{-3}$. The thickness of the dusty gas layer is ~ 100 times lower than the thickness of the dustless gas layer, due to the higher dust opacity. **Lower panels:** The free-free luminosity per logarithmic unit depth as a function of depth, for several values of ν . The calculated emission assumes $\Omega = 0.3$ and $L_{46} = 1$ (scales linearly with both). The emission follows closely the distribution of n_e , with a cutoff at a depth where $\tau_\nu > 1$, and the emission is self-absorbed. At a high enough frequency, the photoionized layer remains optically thin, and most of the observed free-free originates close to the ionization front where n_e peaks.

$L_\nu \propto \nu^2$. For the RPC slab the optically thick spectral slope is somewhat flatter, with $L_\nu \propto \nu^{1.64}$ for dusty gas, and $L_\nu \propto \nu^{1.4}$ for dustless gas. This occurs because the slab is not isothermal, and is composed of different layers at different temperatures, each one with a different ν_{thick} , leading to a total emission which is flatter. The spectral turnover at $\nu < \nu_{\text{thick}}$ moves to lower frequencies as r/r_{dust} increases (Fig. 2).

The value of L_ν in the optically-thin regime of dustless gas decreases with increasing r/r_{dust} , in contrast with the dusty models, where L_ν remains nearly constant. This difference is due to the following. The emitted free-free spectrum is a function of T (eqs. 1 and 8). In dusty gas, the RPC slab structure is mostly set by the dust opacity, which we assume to be independent of T and n . Thus, the T structure of a dusty RPC slab is roughly independent of r/r_{dust} . In dustless gas, the structure is set by the gas opacity which depends on T and n . Thus, the T structure of a slab varies with r/r_{dust} (see fig. 3 in Baskin et al. 2014a). The structure results in a larger value of $L_\nu \sim n^2 r^2 l$, for a given $T \lesssim 10^5$ K, with decreasing r/r_{dust} , and thus the maximum L_ν decreases with r/r_{dust} for dustless gas. At a given distance, a dustless slab has a larger L_ν compared to a dusty slab by ~ 1 dex (see Fig. 3). As noted above, the higher emission

is a result of a larger compression length-scale l of a dustless slab (Section 2).

The free-free luminosity of dustless gas is significantly larger than in dusty gas. However, dustless gas is expected mostly inside the BLR ($r/r_{\text{dust}} < 1$), and since there $\nu_{\text{thick}} > 10^{12}$ Hz, the free-free contribution of dustless gas in the radio regime is likely negligible.

Free-free emission at $\nu < 1$ GHz must come from gas located at $r/r_{\text{dust}} > 10^3$, where the gas is likely to be dusty. Free-free emission at $\nu > 100$ GHz can come from gas located on scales as small as $r/r_{\text{dust}} \sim 10$, which may be dustless (e.g. a failed disc wind). Thus, the $\nu > 100$ GHz regime is where free-free emission from dustless gas is most likely to be detectable.

A superposition of free-free emitting gas clouds extending over a range of distances, say from r_{in} to r_{out} , can produce a spectral slope, α , at a given ν which can be anywhere in the range $\alpha_{\text{thin}} < \alpha < \alpha_{\text{thick}}$, or specifically $-0.1 < \alpha < 1.64$, for ν in the intermediate range $\nu_{\text{thick}}(r_{\text{out}}) < \nu < \nu_{\text{thick}}(r_{\text{in}})$. At $\nu > \nu_{\text{thick}}(r_{\text{in}})$ all contributing gas clouds become optically thin, which gives $\alpha \approx -0.1$, while at $\nu < \nu_{\text{thick}}(r_{\text{out}})$ all clouds are optically thick, and L_ν will fall as fast as $\alpha \approx 1.64$ (dusty gas) or $\alpha \approx 1.4$ (dustless gas). At the intermediate ν values, the emission at a given ν is dominated by the clouds where $\tau_\nu \sim 1$. This allows to measure directly the emitting surface area

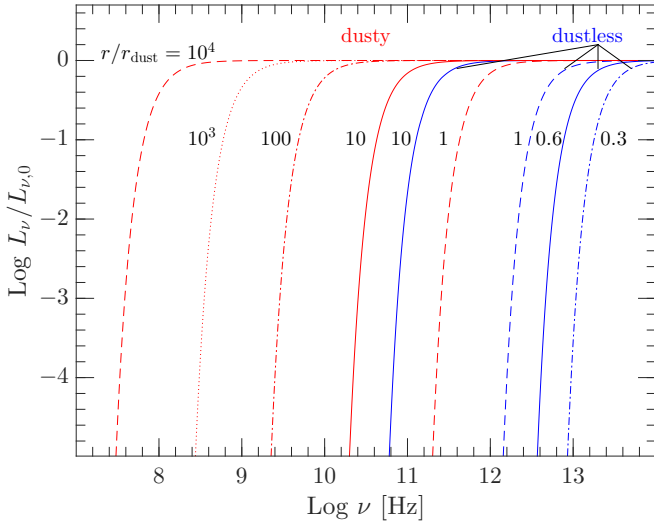


Figure 2. Free-free absorption by dusty and dustless RPC gas located at various distances. The y-axis presents the transmitted luminosity, L_ν , relative to the incident luminosity, $L_{\nu,0}$. The distance is measured in units of r_{dust} . The gas becomes optically thick below the frequency ν_{thick} , which decreases with increasing distance. At a given distance, ν_{thick} of dustless gas is higher than for dusty gas, as the ionized column of dustless gas is larger. Dustless gas at the BLR ($r/r_{\text{dust}} < 1$) becomes optically thick only at $\nu_{\text{thick}} < 3 \times 10^{12}$ Hz (or $\lambda > 100 \mu\text{m}$). Dusty gas at the BLR ($r/r_{\text{dust}} = 1$) becomes thick below 500 GHz, while on the NLR scale ($r/r_{\text{dust}} = 10^3$) it remains optically thin down to 1 GHz.

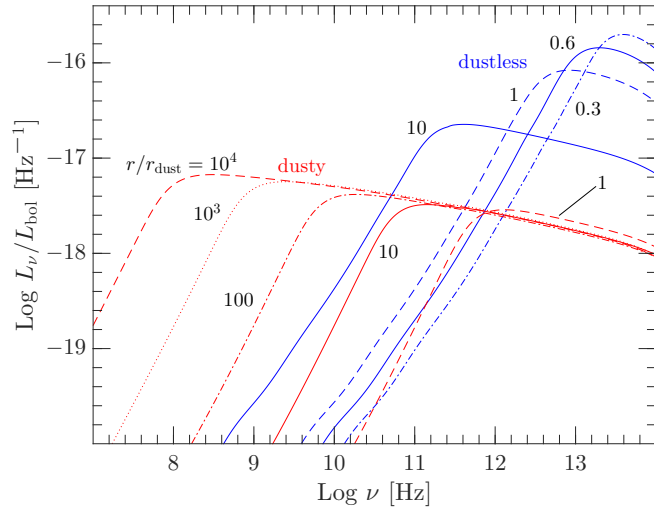


Figure 3. The free-free emission from the illuminated side of a slab located at various distances. The assumed covering factor is $\Omega = 0.3$ at all r . The free-free emission spectral slope turns over from optically thin, $L_\nu \propto \nu^{-0.1}$, to optically thick, $L_\nu \propto \nu^{1.4-1.64}$ (see text), at $\nu < \nu_{\text{thick}}$ (see Fig. 2). The optically thin emission of dustless gas is significantly larger than in dusty gas. Photoionized dustless gas just outside the BLR can contribute significantly only at $\nu > 100$ GHz, while optically thin free-free emission at 1 GHz can come from photoionized gas only at $r/r_{\text{dust}} > 1000$.

of the free-free emitting clouds, based only on the value of L_ν , as further described below.

Figure 4 presents the specific intensity, I_ν , multiplied by 4π , i.e. the flux density emitted by a unit area, assuming isotropic emission. The radiation is produced by the slabs presented in Fig. 3. The solutions for dustless BLR slabs ($r/r_{\text{dust}} \leq 1$) at $\nu < \nu_{\text{thick}}$ all collapse to

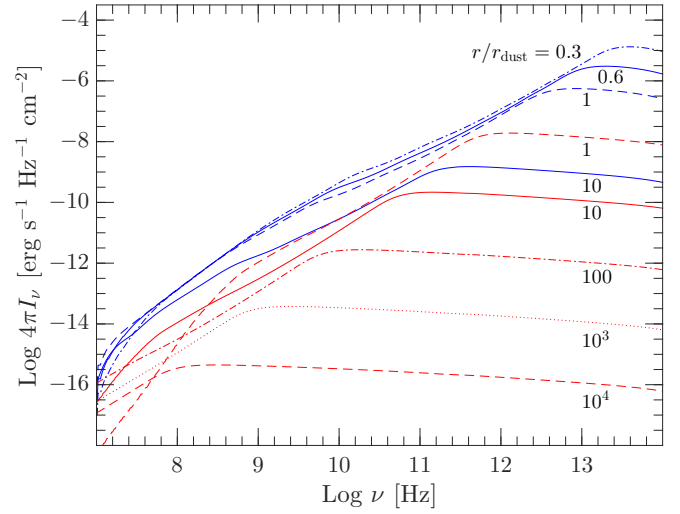


Figure 4. The same as Fig. 3 for the specific intensity I_ν – the flux per solid angle subtended by the emitting gas. The optically thick I_ν approaches the blackbody limit, at the temperature of the free-free emitting region. This maximal intensity, at a given ν , allows to derive the minimal emitting surface area from the observed L_ν . If the gas is optically thin, as implied by the observed spectral slope, the minimal emitting area is larger.

a nearly single solution, which corresponds to the quasi-blackbody emission produced in slabs with similar temperatures. The small range of T results from the limited range of $0.3 \leq r/r_{\text{dust}} \leq 1$ that corresponds to the BLR. The value of I_ν is independent of distance from the central source, and is also independent of L_{bol} . At $\nu > \nu_{\text{thick}}$ the layer becomes optically thin, and I_ν drops below the maximal blackbody value obtained at $\nu < \nu_{\text{thick}}$. The value of the predicted I_ν allows to constrain the minimal possible emitting surface area A , since $L_\nu = A \times \pi I_\nu$.

For dusty gas, which extends over a broader range of values of r/r_{dust} , we get a similar behaviour, although I_ν of the optically-thick gas decreases slightly with increasing distance. This occurs due to the following. The optical depth at a given ν is approximately $\tau_\nu \propto T^{-5/2}(r/r_{\text{dust}})^{-2}$ for $h\nu \ll kT$ (eq. 8), where we use $n \propto T^{-1}(r/r_{\text{dust}})^{-2}$ (Stern et al. 2014a, eq. 6) and $l \propto T(r/r_{\text{dust}})^2$ (eq. 4), and assume that $\bar{\sigma}$ is independent of T and n . Thus, the maximal temperature of a layer which is still optically thick at ν (i.e. $\tau_\nu \approx 1$) decreases with r/r_{dust} , yielding the decrease of I_ν with r/r_{dust} of the optically-thick gas.

Note the spectral break of the $r/r_{\text{dust}} = 1$ gas emission below 1 GHz. This break occurs since $\nu < 10\nu_p$ where we assume $\epsilon_\nu = 0$ (Section 2.2).

If the free-free emitting source is spatially resolved, the value of I_ν can be directly determined. The value of I_ν is conveniently expressed in the radio regime using the brightness temperature, $T_b \equiv I_\nu c^2 / 2\nu^2 k$. An isothermal gas slab at a temperature T_e with an optical depth τ_ν , produces emission with $T_b = T_e(1 - e^{-\tau_\nu})$ (e.g. Rybicki & Lightman 2004). So, for optically thick gas we get blackbody emission, with $T_b = T_e$, and for optically thin gas we get $T_b = T_e \tau_\nu$. Since RPC gas is not isothermal, the derivation of T_b is somewhat less trivial.

Figure 5 presents T_b for the same set of RPC models presented in Fig. 4. A simple and robust conclusion is that a source with $T_b > 3 \times 10^6$ K cannot be produced by free-free emission from RPC gas. Lower maximal values for T_b are possible at $\nu > 1$ GHz. Dusty gas always has a lower T_b than dustless gas, as the ionized column is about a factor of 10 smaller than in dustless gas (~90 per cent of

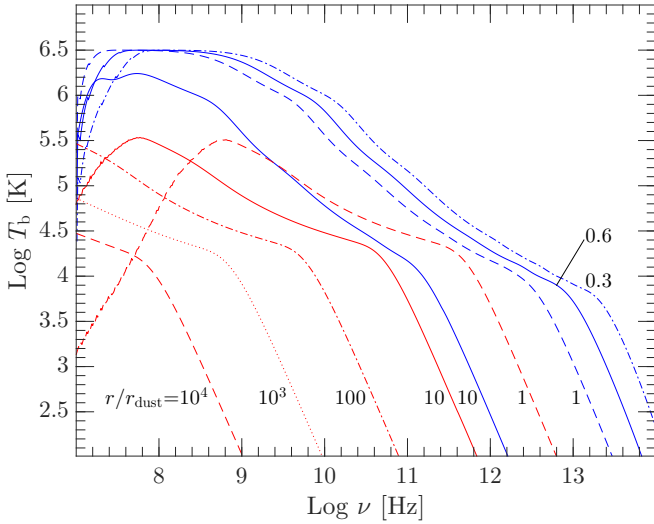


Figure 5. Same as Fig. 4 where I_ν is replaced by $T_b = I_\nu c^2 / 2\nu^2 k$, a convenient way to represent I_ν . At $\nu > \nu_{\text{thick}}$ (see values in Fig. 2), an RPC slab is optically thin, which gives $T_b \propto \nu^{-2}$, as $I_\nu \sim \text{constant}$. At $\nu < \nu_{\text{thick}}$, the slab is optically thick, and $T_b \sim T_e$ at the $\tau_\nu \sim 1$ layer. With decreasing ν , α_ν increases, and thus the $\tau_\nu \sim 1$ layer is found closer to the surface, where the gas is less compressed and T_e is higher. The steep drop at the lowest ν is due to self-absorption below the plasma frequency (eq. 14). In all models $T_b \leq 3 \times 10^6$ K, the Compton temperature of the gas. On scales of $r/r_{\text{dust}} > 10$, which can be resolved in nearby AGN at $\nu > 10$ GHz, the maximal T_b of free-free emission is $\leq 10^5$ K (see also Fig. 9).

the ionizing continuum is absorbed by the dust and is reradiated in the IR). The steep drop in T_b occurs when $\tau_\nu < 1$, as $T_b \propto \tau_\nu$. A shallower drop of T_b occurs in the regime where $\tau_\nu \gg 1$. The drop in T_b with increasing ν occurs as the layer where the $\tau_\nu \sim 1$, which dominates the emission, is thicker and extends inwards to the colder deeper layers where the gas is denser and less ionized.

3.3.2 Back side emission

Figure 6 presents the emitted spectrum from the back side of a dusty or dustless RPC slab, for a range of values of a total H column Σ_H . The slab is located at $r/r_{\text{dust}} = 1$ in all cases. The maximal values of $\Sigma_H = 10^{23.5}$ and 10^{22} cm^{-2} are presented for a dustless and a dusty slabs. Increasing Σ_H further has little effect on the emitted spectrum, since the gas becomes mostly neutral, and does not contribute to the emission or to the absorption ($\epsilon_\nu \approx 0$, $\alpha_\nu \approx 0$).

The value of L_ν in the optically thin regime increases with Σ_H . In the dustless gas the effect can be dramatic, where an increase of Σ_H from 10^{22} to 10^{23} cm^{-2} yields an increase of L_ν by ~ 5 dex. A further increase from $\Sigma_H = 10^{23}$ to $10^{23.5} \text{ cm}^{-2}$ yields only a small rise, as the additional column resides behind the ionization front, and is mostly neutral. A similar, but less dramatic, effect is found for the dusty slab, where L_ν increases by ~ 2 dex when Σ_H increases from 10^{20} to 10^{21} cm^{-2} , with only a small rise when Σ_H increases further to 10^{22} cm^{-2} .

The sharp increase in L_ν in the optically thin dustless gas occurs since $\epsilon_\nu \propto n^2$ (eq. 1), and n rises sharply near the ionization front in dustless gas due to the RPC effect (e.g. Baskin et al. 2014a, fig. 3). In dusty gas, the UV opacity is independent of the gas ionization, and the rise in n , due to the RPC effect, is less sharp (see Stern et al. 2014a, fig. 2; note also that $\tau \propto \Sigma_H$ for dusty gas).

Fig. 6 also shows that ν_{thick} increases with Σ_H . This occurs since n increases with depth, i.e. Σ_H , as the gas compression becomes larger

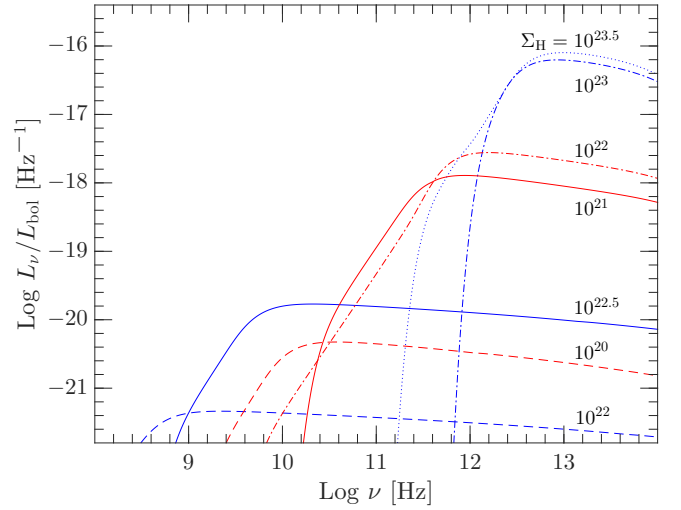


Figure 6. The free-free emission from the back side of a dusty (red) or a dustless (blue) slab, as a function of the slab total H column Σ_H . The slab is located at $r/r_{\text{dust}} = 1$. The optically thin emission increases up to a column of $\Sigma_H \sim 10^{23} \text{ cm}^{-2}$ for dustless gas, and $\sim 10^{21} \text{ cm}^{-2}$ for dusty gas. Above these columns the additional gas resides behind the ionization front, the gas is mostly neutral, and produces little free-free emission or absorption. Most of the emission is produced close to the ionization front since $\epsilon_\nu \propto n_e^2 T^{-1/2}$ (eq. 1), and n_e is highest there, and T is lower. At lower Σ_H , L_ν drops sharply, by a factor of $\sim 10^5$ at $\Sigma_H \sim 10^{22} \text{ cm}^{-2}$ in dustless gas, and by ~ 300 at $\Sigma_H \sim 10^{20} \text{ cm}^{-2}$ for dusty gas. Also, ν_{thick} decreases steeply with decreasing Σ_H , by a factor of ~ 3000 for dustless gas, and by ~ 30 for dusty gas, at the above columns.

inwards in the RPC solution. Thus, as ν_{thick} is set by $\tau_\nu = \alpha_\nu l = 1$, and $\alpha_\nu \propto n^2 \nu^{-2}$ (eq. 9), ν_{thick} increases (the decrease in l with Σ_H is typically smaller than the increase in n ; e.g. Baskin et al. 2014a, figs 1 and 2). The drop in L_ν at $\nu < \nu_{\text{thick}}$ is very sharp, in particular for the dustless gas. This occurs since the observed radiation comes only from the $\tau_\nu \sim 1$ layer, and the thickness of this layer drops with decreasing ν as $\alpha_\nu^{-1} \propto \nu^2$. At $\nu > \nu_{\text{thick}}$, we get $\tau_\nu < 1$ throughout the slab, and the emission is isotropic.

3.4 Comparison with uniform density models

How do the RPC results presented above differ from the predicted free-free emission of the commonly assumed uniform-density gas clouds?

Figure 7, and Figure 8, compare the calculated free-free emission of uniform-density dustless slab, and dusty slab, respectively, with that of an RPC slab located at the same distance. The emitted spectrum is calculated from the illuminated side. In uniform density models the gas density, or equivalently the ionization parameter, need to be assumed. The dustless models (Fig. 7) are evaluated for $-3 \leq \log U \leq 1$ at $r/r_{\text{dust}} = 1$. The associated gas density is $\log n = 8.57 - \log U$. The dusty models (Fig. 8) are evaluated at $r/r_{\text{dust}} = 10^4$ for $-3 \leq \log U \leq 0$, where the associated density is $\log n = 0.57 - \log U$.

The uniform density models predict emission spectra which depend on the value of U . The optically thin emission decreases with increasing U in both dusty and dustless gas. This occurs for the following reason. The optically thin emission follows $L_\nu \propto \epsilon_\nu l$, where $\epsilon_\nu \propto T^{-1/2} n^2$ (eq. 1). In the dustless slab, the column of the ionized layer satisfies $ln \propto U$. Thus, $L_\nu \propto T^{-1/2} n U \propto T^{-1/2} n_\gamma$, or $L_\nu \propto T^{-1/2}$, at a given r where n_γ is fixed. The rise in L_ν with de-

creasing U in dustless uniform density gas (Fig. 7) therefore occurs because of the drop in T .

In dusty gas, the ionized column ln for $\log U > -2$ is set by the dust UV opacity, which is constant. Thus, $L_\nu \propto T^{-1/2}n \propto T^{-1/2}U^{-1}$, which leads to a steeper drop in L_ν with increasing U . For $\log U \leq -2$ the gas opacity dominates, so the increase in L_ν with decreasing U becomes smaller, and is similar to the change in dustless gas.

The transition to optically thick emission occurs at ν_{thick} , where $\tau_\nu = \alpha_\nu l = 1$. Since $\alpha_\nu \propto T^{-3/2}n^2\nu^{-2}$ (eq. 9), and in dustless gas $ln \propto U$, we get $\tau_\nu \propto T^{-3/2}\nu^{-2}$, which gives $\nu_{\text{thick}} \propto T^{-3/4}$ at the $\tau_\nu \sim 1$ layer. Thus, ν_{thick} decreases with increasing U since T increases. In dusty gas at $\log U > -2$ the ionized column ln is constant, which gives $\nu_{\text{thick}} \propto T^{-3/4}n^{1/2}$, which results in a somewhat steeper drop of ν_{thick} with increasing U .

The spectral slope of the optically thick emission of dustless gas at $\log U \leq 0$ is close to 2, the Rayleigh-Jeans slope of blackbody emission. This reflects the small temperature gradient within a uniform density ionized slab. The optically thick slope becomes somewhat flatter for $\log U = 1$, reflecting the increase in T close to the surface where $T \sim 10^5$ K (compared to $T \sim 10^4$ K inwards). The superposition of free-free emission at different temperatures leads to the spectral flattening. In dusty gas, the optically thick emission shows less structure, as the slab structure is set by the fixed dust opacity, which leads to a more isothermal structure.

The comparison above highlights the advantage of the RPC solution. Apart from being more realistic, the predicted gas emission is set only by a single free parameter, r/r_{dust} . The distance of the photoionized gas can sometimes be observationally determined (see below), which then leaves no free parameters. In contrast, the uniform density model predictions depend on an additional free parameter, n , or U . The attempts to determine U from line emission observations imply that it spans a broad range of values (Baldwin et al. 1995), a range which naturally results from the RPC effect (Baskin et al. 2014a; Stern et al. 2014b).

Figure 9 presents the maximal possible brightness temperature T_b of uniform density slabs at a range of distances. As in the RPC case (Fig. 5), the maximal value is $T_b \sim 3 \times 10^6$ K, and is achieved only at $\nu < 1$ GHz, and for extremely compact clouds at $r \sim r_{\text{dust}}$. Radio emission with $T_b > 10^6$ K at $\nu > \text{a few GHz}$, cannot be generally produced by photoionized gas, regardless of the gas location or density. In fact, such T_b values cannot be produced by free-free emission of hot gas in RQ AGN in general, regardless of the gas heating mechanism, as further discussed below.

4 COMPARISON WITH OBSERVATIONS

4.1 Free-free absorption

Free-free absorption of a background continuum source produces a sharp spectral break below a certain frequency, ν_0 , with a flux drop of the form $L_\nu \propto e^{-(\nu_0/\nu)^2}$. This is in contrast with the spectral break due to self-absorption of either a free-free source, or a synchrotron source, which produces a power-law (PL) below the spectral break frequency, with $L_\nu \propto \nu^2$ or $L_\nu \propto \nu^{2.5}$ (e.g. Rybicki & Lightman 2004). Thus, free-free absorption has a unique characteristic. In addition, free-free absorption can be easy to detect, if it occurs in front of a high-brightness-temperature background source, which is often present in radio loud AGN. A sharp spectral break below some frequency, suggestive of free-free absorption, is indeed detected in some radio loud AGN (Gopal-Krishna et al. 2014; Callingham et al. 2017; Mhaskey et al. 2019), and is sometimes spa-

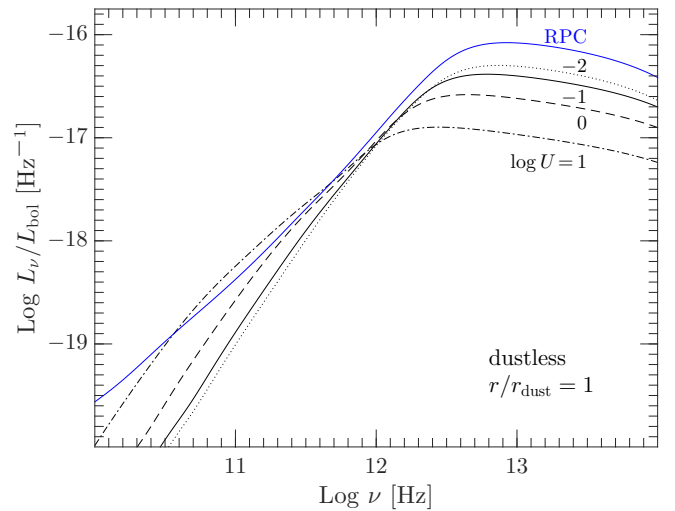


Figure 7. Comparison of the free-free emission of RPC gas with the emission of uniform density gas with various U values. The gas is dustless and is situated at $r/r_{\text{dust}} = 1$, where $\log n = 8.57 - \log U$. The emission of a uniform density slab depends on the assumed value of U , in contrast with the RPC solution which is uniquely set by the distance. The optically thick emission of the uniform density gas generally shows a steeper ($\alpha \sim 2$) optically thick emission, compared to RPC gas. This occurs since a uniform density slab is closer to being isothermal, compared to the RPC slab, which is effectively composed of a superposition of layers with decreasing T inwards, leading to a flatter slope ($\alpha \sim 1.64$, Fig. 3).

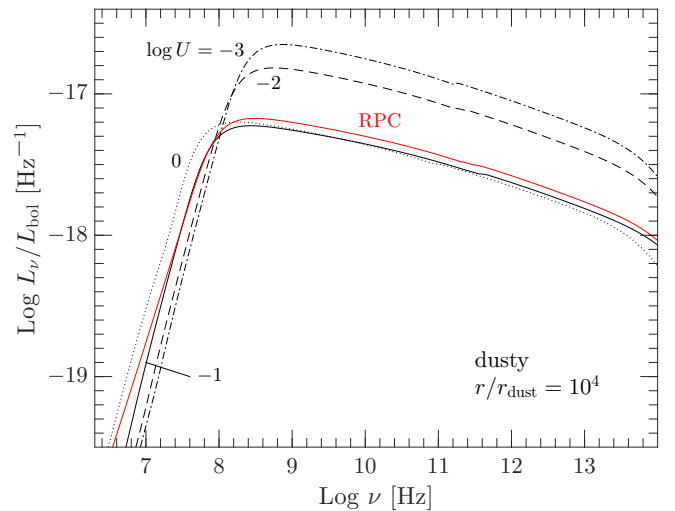


Figure 8. Same as Fig. 7 for a dusty slab at $r/r_{\text{dust}} = 10^4$, with various values of U , compared to an RPC slab at the same distance. The density is $\log n = 0.57 - \log U$. The optically thin spectral slope is similar for all models, and the optically thick RPC spectral slope is only slightly flatter than the slope of the constant density slab.

tially resolved in high resolution observations (e.g. Vermeulen et al. 1994; Walker et al. 1994; Levinson et al. 1995; Ulvestad et al. 1999; Ulvestad 1999; Gallimore et al. 1999; Pedlar et al. 1998; Walker et al. 2000; Jones et al. 2001; Marr, Taylor, & Crawford 2001; Kamenno et al. 2003). Below we discuss a few well studied cases in nearby AGN, and their consistency with the RPC model predictions for a free-free absorption screen.

Apparently the best studied free-free absorption case is in NGC 1275 (3C 84), a radio loud active galaxy in the centre of

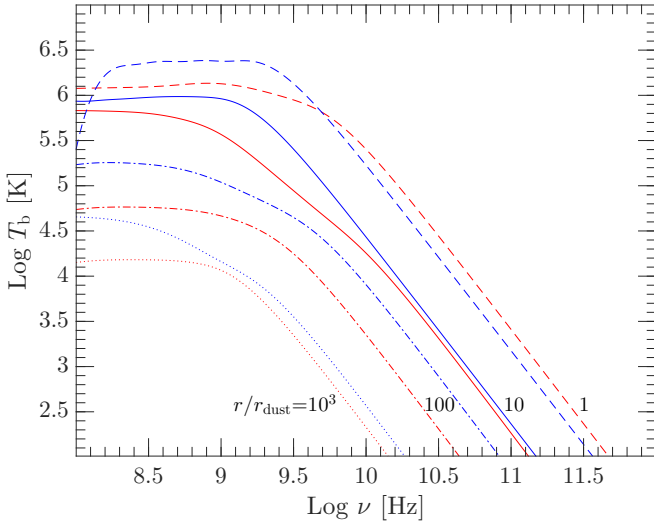


Figure 9. Same as Fig. 5 for a constant density slab. At each value of r/r_{dust} we present the dustless and dusty slabs with the value of U which leads to the maximal value of T_b . These are generally the highest U and highest τ_ν slabs which can physically fit within the available r . These criteria lead to the highest T_c close to the surface (where $\tau_\nu = 1$), as required since $T_b \leq T_c$. A radio source with $T_b > 10^6$ K at $\nu >$ a few GHz cannot be produced by free-free emission of photoionized gas, regardless of the gas confinement mechanism (see also Fig. 5).

the Perseus cluster. High angular resolution VLBA observations at 5 GHz showed historically a single sided jet, as commonly observed in highly beamed sources pointing at us. However, followup VLBA observations at 15 and 22 GHz revealed a counter jet 6–8 mas to the north, a feature which is free-free absorbed at lower frequencies (Vermeulen et al. 1994; Walker et al. 1994). The free-free absorbing screen is likely in a disc configuration, lying in front of the counter jet, and behind the jet directed at us (Vermeulen et al. 1994; Walker et al. 1994). Is the free-free absorbing screen composed of photoionized gas? If yes, is the optical depth of the screen, which is spatially resolved in this object, consistent with the distance versus absorption frequency relation of RPC gas?

The absorption is spatially resolved with a projected distance on the sky of 2–2.5 pc from the centre (Vermeulen et al. 1994; Walker et al. 1994; Levinson et al. 1995; Walker et al. 2000). The jet is inclined at $\theta \sim 65^\circ$ to the line of sight (Fujita & Nagai 2017). If the absorbing screen is a disc at right angle to the jet, then the projected absorber distance corresponds to a physical distance along the disc of 4.7–5.9 pc from the ionizing source. The bolometric luminosity of NGC 1275 is $L_{\text{bol}} \approx 4 \times 10^{44}$ erg s $^{-1}$ (section 2.2 in Levinson et al. 1995), which gives $r_{\text{dust}} = 0.04$ pc (eq. 11). Thus, the absorbing gas resides at a deprojected distance of $r/r_{\text{dust}} \approx 120 - 150$. The photoionized RPC gas gives $\nu_{\text{thick}} \approx 5.2 - 6.4$ GHz for dusty gas, and $\nu_{\text{thick}} \approx 4.1 - 5.6$ GHz extrapolated for dustless gas, using the relations in eq. 21. The observations yield $\tau_{8 \text{ GHz}} \approx 2$ (Levinson et al. 1995), which implies $\nu_{\text{thick}} \approx 11$ GHz, which agrees within a factor of two with the predicted values. Thus, the free-free screen observed in NGC 1275 is consistent with RPC photoionized gas, where both the ionization structure and the density structures are set by the illuminating ionizing radiation.

A similar spatially resolved free-free absorber is detected in NGC 4151, where Pedlar et al. (1998) detected free-free absorption with $\nu_{\text{thick}} \approx 300$ MHz of an extended radio source located ~ 50 pc from the centre. This AGN shows significant long term variability, with

a typical flux of $F_\lambda(5100\text{\AA}) = 4 \times 10^{-14}$ erg s $^{-1}$ cm $^{-2}$ \AA $^{-1}$ measured 20 years prior to the radio observations (Onken et al. 2007). This luminosity may not represent the luminosity ~ 150 years ago, which is illuminating now the screen. However, this luminosity implies $\log L_{\text{bol}} \approx 43.6$, and thus $r_{\text{dust}} \approx 0.013$ pc. The absorber therefore extends over a distance of $r/r_{\text{dust}} \sim 3850$. The RPC predicts $\nu_{\text{thick}} \approx 240$ MHz, consistent with the observed $\nu_{\text{thick}} \approx 300$ MHz.

Another object where the free-free absorption is spatially resolved is NGC 4261, where $\tau_{5 \text{ GHz}} < 1$ at $r > 0.5$ pc (Jones et al. 2001). The estimated $\log L_{\text{bol}} \approx 41.8$ (Eracleous et al. 2010) implies $r_{\text{dust}} \approx 1.65 \times 10^{-3}$ pc, and therefore the observations indicate that $\tau_{5 \text{ GHz}} < 1$ at $r/r_{\text{dust}} > 300$. This result is consistent with the RPC prediction that $\tau_{2.6 \text{ GHz}} = 1$ for $r/r_{\text{dust}} = 300$.

The case of NGC 1052 is particularly interesting (Kameno et al. 2003), as the observations show a clear rise in ν_{thick} with decreasing distance from the centre. Specifically, fig. 3 in Kameno et al. (2003) suggests that $\nu_{\text{thick}} \sim 3, \sim 6$ and ~ 20 GHz, at projected distances of $\sim 1.7, \sim 0.9$ and ~ 0.4 pc from the centre (using the 0.1 pc/mas scaling in this nearby galaxy). The estimated $\log L_{\text{bol}} \approx 43.15$ (using $L_{\text{bol}} = 10L_X$ and L_X from Cusumano et al. 2010), gives $r_{\text{dust}} \approx 7.5 \times 10^{-3}$ pc. Thus, the projected distances are $r/r_{\text{dust}} \sim 225, 120$ and 53, and the RPC predicted values for ν_{thick} are 3.5, 6.4 and 13.9 GHz, which agree well with the above estimated values of $\sim 3, \sim 6$ and ~ 20 GHz. Clearly, a further study of this object is warranted.

4.2 Free-free absorption and emission in NGC 1068

Possible detection of free-free emission was made in NGC 1068, the archetype of obscured AGN. High resolution VLBA observations at 1.4–8.4 GHz revealed a compact nuclear source, which extends on a scale of ~ 10 mas, at right angle to the large scale outflow. The emission spectrum is a flat PL with $\alpha = -0.17 \pm 0.24$ at 5–8.4 GHz, with $T_b \approx 4 \times 10^6$ K (Gallimore, Baum & O’Dea 1997; Roy et al. 1998; Gallimore et al. 2004). This feature was interpreted as free-free emission from highly photoionized gas which covers the surface of the obscuring torus gas, a layer produced by the X-ray illumination of the central ionizing source. However, this PL component cannot be produced by free-free emission, as further described below.

The compact ~ 10 mas scale PL source is characterised by $\langle T_b \rangle = 4 \times 10^6$ K at 5 GHz, with a peak value of 8.6×10^6 K. The emission is interpreted as free-free emission from photoionized gas located at the surface of the obscuring torus (Gallimore, Baum & O’Dea 1997; Roy et al. 1998; Gallimore et al. 2004). The size of ~ 10 mas corresponds to $r \sim 0.7$ pc, or $r/r_{\text{dust}} \sim 5 - 18$ for the range of possible values of L_{bol} (see below). However, RPC photoionized gas is limited to a maximal value of $T_b = 2 \times 10^5$ K at 5 GHz (Fig. 5).

The solution for a uniform density photoionized gas is bound by an even lower value of $T_b < 10^5$ K (Fig. 9). We conclude that the observed high T_b value generally cannot be produced by free-free continuum from photoionized gas. The ~ 10 mas core emission is therefore likely synchrotron emission. Given the low T_b , the synchrotron source is optically thin, and the intrinsic PL slope is therefore expected to be significantly steeper than the observed $\alpha = -0.17$. The observed flat slope is potentially just an artefact produced by a free-free absorption observed below 4 GHz, as further discussed below.

Figure 10, left panel, shows the observed VLBA luminosity density at 5 and 8.4 GHz. There is a sharp spectral turnover below 5 GHz, with only an upper limit at 1.4 GHz. The resolution matched flux densities at 1.4, 5 and 8.4 GHz are $< 0.7, 5.9$ and 5.4 mJy, respectively (Gallimore et al. 2004), implying slopes of $\alpha_{1.4-5} > 1.67$ and $\alpha_{5-8.4} = -0.17$. The observed spectral turnover from above

to below 5 GHz is too sharp to match a self-absorbed free-free source (Fig. 3), and requires the presence of a foreground absorbing screen (Fig. 2). Assuming an unabsorbed PL source with the observed slope of $\alpha = -0.17$ extends down to 1.4 GHz, implies an unabsorbed 1.4 GHz flux of 7.3 mJy, and therefore $\tau_{1.4 \text{ GHz}} \geq 2.3$. This optical depth is consistent with a dusty RPC absorber located at $r/r_{\text{dust}} = 975$. Since free-free absorption follows $\tau_{\nu} \propto \nu^{-2}$ (eq. 9), this screen also produces $\tau_{5 \text{ GHz}} \geq 0.18$, and $\tau_{8.4 \text{ GHz}} \geq 0.06$, so the observed value of $\alpha_{5-8.4} = -0.17$ is also affected by the free-free absorbing screen. The unabsorbed $\alpha_{5-8.4}$ is steeper by $\Delta\alpha = 0.24$ than the observed slope (see Fig. 10). Thus, the implied intrinsic PL slope is $\alpha = -0.41$, which is too steep to be free-free PL emission, regardless of the gas heating mechanism.

The intrinsic slope of the absorbed PL source can also be significantly steeper, if the absorber is located slightly inwards. For example, the observed $\alpha_{5-8.4} = -0.17$ can be produced by a PL source with $\alpha = -0.9$, a typical slope for an optically thin synchrotron source, if the absorber is located at $r/r_{\text{dust}} = 915$ ($\Delta\alpha = 0.73$), as demonstrated in Fig. 10.

Thus, the observed sharp spectral break below 5 GHz requires a foreground free-free absorbing screen. The absorption below 5 GHz implies that the absorption corrected $\alpha_{5-8.4}$ is steeper than observed, which excludes free-free emission as the origin of the observed PL at 5 – 8.4 GHz.

The physical distance of the foreground screen, r , which resides at $r/r_{\text{dust}} = 975$, can be derived from the value of r_{dust} , which is set by L_{bol} . In NGC 1068, $L_{\text{bol}} = 0.4 - 4.7 \times 10^{45} \text{ erg s}^{-1}$ (Gravity Collaboration et al. 2020), which implies $r_{\text{dust}} = 0.04 - 0.14 \text{ pc}$ (eq. 11). The absorber then resides at $r \sim 40 - 140 \text{ pc}$. If this is also the typical lateral dimension of the absorber, it corresponds to an angular scale of 0.5 – 2 arcsec. This large extent is consistent with the similar free-free absorption also observed in component C, which resides 0.3 arcsec to the north of the centre (Gallimore et al. 2004). The VLA observations of component C at 8 – 22.5 GHz reveal a steep PL with $\alpha_{8-22.5} = -0.67$ (Gallimore et al. 1996), but it shows $\alpha_{5-8.4} = -0.23$ (Gallimore et al. 2004), again consistent with the spectral flattening close to the free-free cutoff observed below 5 GHz, which is similar to the observed VLBA scale absorption.

The free-free absorber screen should produce some free-free emission; is this emission detectable? RPC predicts a well defined value for the free-free L_{ν}/L_{bol} at a given r/r_{dust} and Ω (Fig. 3). For the above values of L_{bol} , r/r_{dust} and Ω ($= 0.3$), the RPC model predicts $L_{5 \text{ GHz}} = 2 \times 10^{27} - 2.4 \times 10^{28} \text{ erg s}^{-1} \text{ Hz}^{-1}$. The observed VLBA value is $L_{5 \text{ GHz}} = 1.5 \times 10^{27} \text{ erg s}^{-1} \text{ Hz}^{-1}$. However, the observed VLBA scale emission is not relevant, as the absorber screen emission is expected to extend over an angular scale of ~ 0.5 to 2 arcsec, and the screen emission within the tiny VLBA scale of $\sim 10 \text{ mas}$ is only $\sim 10^{24} \text{ erg s}^{-1} \text{ Hz}^{-1}$. Thus, the absorber free-free emission on the VLBA scale is negligible compared to the compact source emission. Is there evidence for free-free emission on larger scales?

Figure 10, right panel, shows the observed emission on scales of $\sim 100 - 200 \text{ mas}$ from the nucleus. The spectral slope is $\alpha = -0.08$ (Gallimore et al. 1996), which matches well free-free emission. The plot also shows the free-free emission expected from the above derived position of the free-free absorber, $r/r_{\text{dust}} = 915$ and 975. The amplitude of the free-free luminosity implies that the luminosity absorbed by the screen is $\Omega L_{\text{bol}} = 4.9 \times 10^{44} \text{ erg s}^{-1}$. The estimated $L_{\text{bol}} = 0.4 - 4.7 \times 10^{45} \text{ erg s}^{-1}$ implies $\Omega \sim 0.1 - 1$ for the screen. The value of Ω can also be estimated from the known geometry of the system. The observed projected size of the free-free emitter is $h \sim 10 \text{ pc}$, and its distance from the centre, based on RPC is

$r \sim 40 - 140 \text{ pc}$ (see above). If the absorber forms a torus like structure then $\Omega \sim h/r$, or $\Omega \sim 0.07 - 0.25$, which overlaps $\Omega \sim 0.1 - 1$ derived above from the free-free emission amplitude.

To summarize, the $\sim 10 \text{ mas}$ flat PL nuclear source is too bright and too steep to be free-free emission, and is likely optically thin synchrotron emission. The emission is clearly absorbed by a free-free screen located at $r/r_{\text{dust}} \sim 1000$. The free-free emission of this screen is apparently detected on larger scales of 100 – 200 mas. This large scale RPC free-free emitting screen is likely also the source of the spatially resolved X-ray emission lines in NGC 1068 (Ogle et al. 2003). The X-ray emission lines luminosity and their relative strengths are also well matched by RPC emission (Bianchi et al. 2019).

4.3 Exclusion of free-free emission from hot gas

Above we excluded photoionization, either of RPC gas or of uniform density gas, as the heating mechanism for the $\sim 10 \text{ mas}$ PL component observed in NGC 1068. Can radio emission with $T_{\text{b}} \sim 4 \times 10^6 \text{ K}$ generally be produced by free-free emission of hot gas? Below we show that in AGN such hot gas over predicts the observed X-ray emission.

In order to show that, we first estimate the required gas T_{e} , in order to produce the observed T_{b} . If the gas is optically thick at 5 GHz, then $T_{\text{e}} = T_{\text{b}}$. But, the thermal radio emission of optically thick gas is blackbody, that is a PL with $\alpha = 2$, while the observed slope is $\alpha_{5-8.4} = -0.17 \pm 0.24$ (Gallimore et al. 2004). The hot gas therefore needs to be optically thin, in which case $T_{\text{e}} = T_{\text{b}}/\tau_{\nu}$. The minimal T_{e} requires the largest possible τ_{ν} , which is consistent with the observed $\alpha_{5-8.4}$. The largest acceptable value is $\tau_{5 \text{ GHz}} = 0.1$, as it produces free-free emission with $\alpha_{5-8.4} = 0.06$, which is within the acceptable range of $\alpha_{5-8.4} = -0.17 \pm 0.24$. Thus, the observed $T_{\text{b}} \sim 4 \times 10^6 \text{ K}$ and the constraint $\tau_{\nu} < 0.1$ implies $T_{\text{e}} > 4 \times 10^7 \text{ K}$.

Can the core radio emission in NGC 1068, and generally the radio emission in radio-quiet AGN, be produced by free-free emission from $T_{\text{e}} > 4 \times 10^7 \text{ K}$ gas? Figure 11 presents the calculated free-free emission of gas at $T_{\text{e}} = 4 \times 10^7 \text{ K}$, with $\tau_{5 \text{ GHz}} = 0.1$, and thus $T_{\text{b}}(5 \text{ GHz}) = 4 \times 10^6 \text{ K}$, as observed in the core of NGC 1068. The free-free emission is overlaid on the mean SED of type 1 AGN (Richards et al. 2006), by matching their $\nu L_{5 \text{ GHz}}$. The free-free emission peaks at $\nu \sim 10^{18} \text{ Hz}$, or an energy of $h\nu \sim 3 \text{ keV}$. Clearly, the implied free-free X-ray luminosity far exceeds the observed X-ray luminosity. Specifically, the free-free emission gives $L_{2 \text{ keV}}/\nu L_{5 \text{ GHz}} \sim 10^7$, compared to the observed mean AGN SED which is characterised by $L_{\text{X-ray}}/\nu L_{\text{Radio}} \sim 10^5$, or equivalently $L_{2 \text{ keV}}/\nu L_{5 \text{ GHz}} \sim 1.6 \times 10^4$ (using the X-ray bolometric correction factor $L_{\text{X-ray}} = 6.25 L_{2 \text{ keV}}$ from Laor & Behar 2008). The hot free-free emitting gas over produces the X-ray luminosity by a factor of ~ 600 .

The above argument applies for an average unobscured AGN. In NGC 1068 the X-ray emission is obscured, and the absorption corrected value is estimated in the range of $L_{2 \text{ keV}} = 0.2 - 4 \times 10^{43} \text{ erg s}^{-1}$, assuming a PL with a slope of -1 (Gravity Collaboration et al. 2020, and references therein). The luminosity of the $T_{\text{b}} = 4 \times 10^6 \text{ K}$ source is $\nu L_{5 \text{ GHz}} = 7.5 \times 10^{36} \text{ erg s}^{-1}$, and if this is free-free emission of hot gas, it implies $L_{2 \text{ keV}} = 7.5 \times 10^{43} \text{ erg s}^{-1}$, which is about twice the estimated intrinsic $L_{2 \text{ keV}}$.

An additional difficulty to accommodate the free-free X-ray emission is its spectral shape. The observed X-ray spectral shape in AGN is a PL with a slope of ~ -1 , in contrast with the free-free SED of

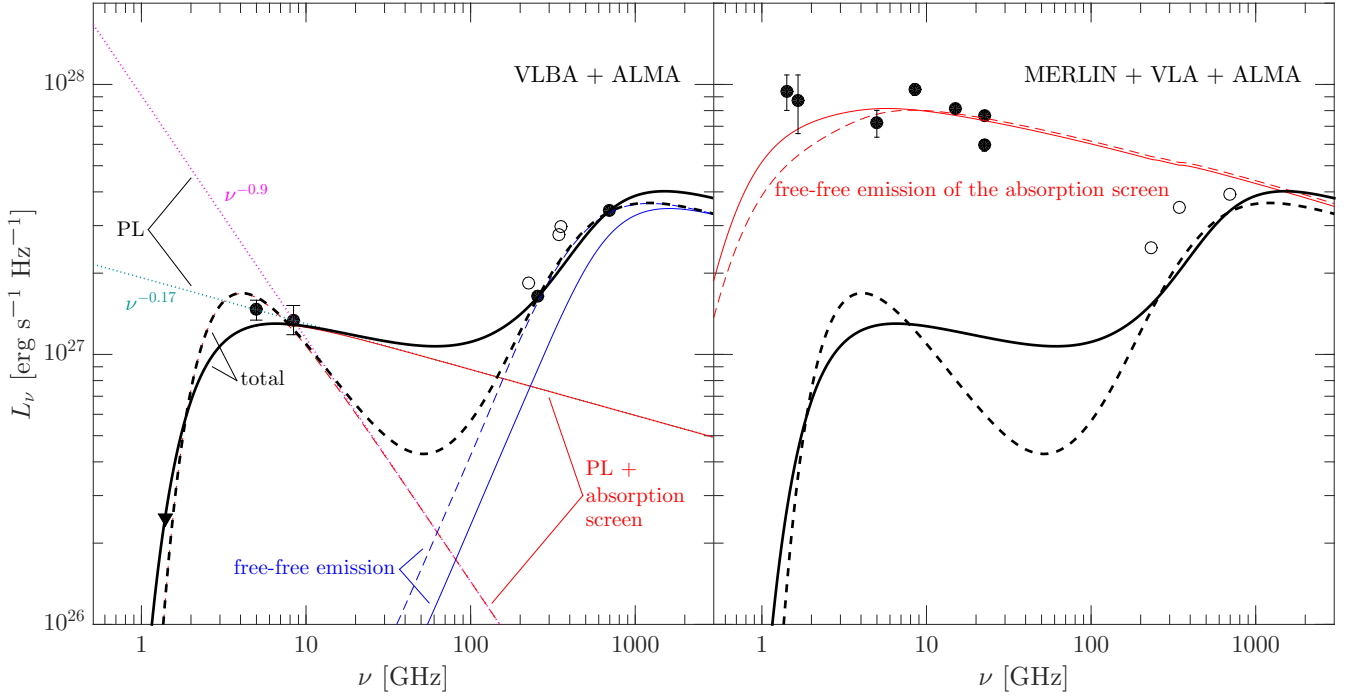


Figure 10. The mas scale (left panel) and sub-arcsec scale (right panel) core radio emission in NGC 1068. **Left panel:** VLBA observations below 10 GHz of the central emission feature (S1) which has a size of $\sim 5 - 15$ mas (Gallimore et al. 2004). ALMA observations above 100 GHz, with a resolution of $\sim 20 - 60$ mas. The filled dots are from García-Burillo et al. (2016) and Impellizzeri et al. (2019), and the circles from Inoue et al. (2020). The sharp spectral turnover below 5 GHz indicates a free-free absorption screen. The absorbed PL may be as flat as -0.17 (dotted cyan line) with a dusty RPC absorber located at $r/r_{\text{dust}} = 975$ (solid black line), or it can be a steep PL with a slope of -0.90 (dotted magenta line) with an absorber at $r/r_{\text{dust}} = 915$ (dashed line). The excess emission above 100 GHz is well fit by free-free emission of RPC photoionized dustless gas, located either at $r/r_{\text{dust}} = 3.1$ with $\Omega = 0.025$ for $\alpha = -0.17$ (solid lines), or at $r/r_{\text{dust}} = 4.2$ with $\Omega = 0.03$ for $\alpha = -0.9$ (dashed lines). **Right panel:** the more extended nuclear emission on scales of 100 – 200 mas, derived from MERLIN and VLA observations (Gallimore et al. 1996). The relative strength of this more extended free-free emission implies $\Omega \sim 0.1 - 1$, which is comparable to the values expected from the estimated distance and size of the free-free absorbing screen.

a PL with a slope of ~ -0.1 with a thermal cutoff at ~ 3 keV. In addition, the values of $\tau_{5 \text{ GHz}}$ and $L_{5 \text{ GHz}}$ in NGC 1068, together with eqs. 6 and 9 allow to derive the density and size of the free-free emitting region, which gives $n_e = 2 \times 10^6 \text{ cm}^{-3}$, and a size of 0.6 pc. The size is in sharp contrast with the typical size of the X-ray emitting region in AGN of $\sim 10^{-3}$ pc.

To summarize, radio emission component in AGN with $T_b > 10^6$ K at 5 GHz can be free-free emission only if the radio is weak enough to satisfy $\nu L_{5 \text{ GHz}}/L_{2 \text{ keV}} < 10^{-7}$, so it does not dominate the X-ray emission. Such a source produces less than ~ 1 per cent of the radio emission at 5 GHz. Otherwise, the observed X-ray emission becomes dominated by the free-free emission, which is inconsistent with the observed spectral slope and size of the X-ray emitting region (likely produced in a corona above the innermost accretion disc). Significant radio emission with $T_b > 10^6$ K in radio-quiet AGN is therefore likely to be synchrotron emission.

A synchrotron source requires relativistic electrons with $\gamma \gg 1$, and thus kinetic energy $\gg m_e c^2$. If the source is optically thick it will inevitably have $T_b \gg 10^9$ K. A synchrotron source with $T_b < 10^9$ K is most likely optically thin, and is thus expected to produce steep PL emission. In NGC 1068, the observed flat $\alpha_{5-8.4}$ is most likely just an artefact of the free-free absorption screen, which becomes dominant around 5 GHz. The free-free absorption corrected radio slope is $\alpha_{5-8.4} < -0.5$, which is consistent with optically thin synchrotron emission.

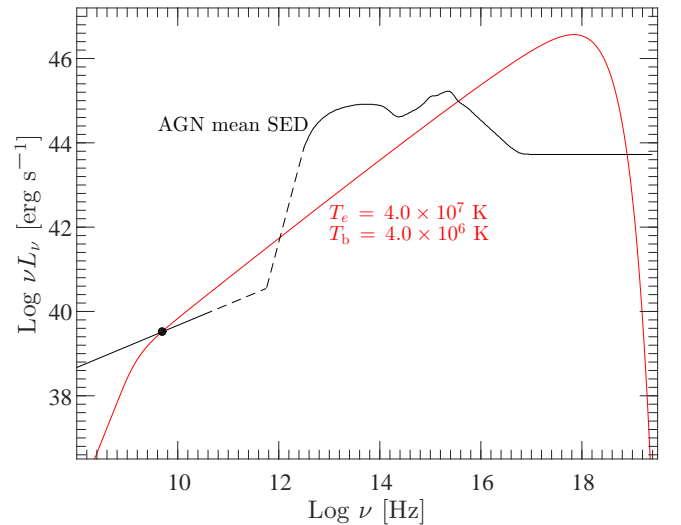


Figure 11. The free-free emission of hot gas with $T_e = 4 \times 10^7$ K (red line), which produces a high-brightness-temperature radio emission with $T_b = 4 \times 10^6$ K at 5 GHz, as observed in NGC 1068. Such a source produces $L_{2 \text{ keV}}/\nu L_{5 \text{ GHz}} = 10^7$, which is a factor of 600 larger than typically observed in radio quiet AGN (Laor & Behar 2008). Thus, if a significant fraction of the observed radio emission at 5 GHz is characterised by $T_b > 10^6$ K, the emission cannot be thermal free-free emission of hot gas, and is inevitably synchrotron emission.

4.4 Free-free emission in other active galaxies

Mundell et al. (2000) searched for free-free continuum on the mas scale in five nearby Seyfert galaxies. In four of these, $T_b > 10^8$ K, which excludes free-free emission (see above). In NGC 4388, the non detection of mas scale emission places an upper limit of $T_b < 2.2 \times 10^6$ K, which is consistent with free-free emission. However, followup VLBI observations at 1.6 and 5 GHz by Giroletti & Panessa (2009) find a spectral slope of $\alpha < -0.7$, which excludes core free-free emission. The flat spectrum emission detected on ~ 50 –100 mas scale in NGC 4388 with MERLIN, may well be produced by free-free emission on scales of 5–1 pc (Mundell et al. 2000).

Of the four additional faint Seyfert nuclei observed by Giroletti & Panessa (2009), NGC 5033 shows the expected free-free slope of $\alpha = -0.1 \pm 0.1$, but its $T_b > 1.3 \times 10^7$ K excludes the free-free interpretation.

The most, and maybe only, convincing detection of free-free emission is from the nucleus of Cygnus A. Carilli et al. (2019) detected flat PL emission, with $\alpha = -0.1$ from 18 to 48 GHz, from a torus structure with a size of ~ 500 pc. The torus resides perpendicular to the radio loud jet. The observed radio intensity at 34 GHz gives $T_b = 240$ K at 100 mas, which corresponds to a distance of 120 pc from the centre. The bolometric luminosity of Cygnus A is $0.5 - 2 \times 10^{46}$ erg s $^{-1}$ (Tadhunter et al. 2003), which implies $r_{\text{dust}} \sim 0.2$ pc, and thus T_b is measured at $r/r_{\text{dust}} \sim 600$. An RPC free-free emitting dusty gas at $r/r_{\text{dust}} \sim 600$ is expected to remain optically thin down to ~ 1.4 GHz (eq. 21), which is consistent with the observed optically thin emission down to 18 GHz (Carilli et al. 2019). However, since $\tau_\nu \propto \nu^{-2}$, we expect that $\tau_{34 \text{ GHz}} \sim 2 \times 10^{-3}$, which implies a predicted $T_b = \tau T_e \sim 20$ K for photoionized gas (see also Fig. 5), in contrast with the observed value of 240 K. Also, for an estimated total flux density from the torus of ~ 2 mJy, we get that $L_\nu/L_{\text{bol}} = 5 \times 10^{-17}$ at 34 GHz, compared to the predicted RPC value of $L_\nu/L_{\text{bol}} = 4 \times 10^{-18}$ (Fig. 3). Again, the predicted free-free emission from AGN photoionized gas is a factor of ~ 10 too low. If the free-free emitting gas is dustless, then L_ν/L_{bol} is a factor ~ 10 larger (Fig. 3), and is consistent with the observed ratio. Dustless gas at such a high r/r_{dust} of ~ 600 would suggest the gas originates from a gas outflow which starts at $r/r_{\text{dust}} < 1$, possibly related to the jet activity in this RL AGN. Alternatively, other local gas heating mechanism, such as star formation, or mechanical jet heating, may also boost the free-free intensity to the observed value.

The two critical points for the successful detection of free-free emission in Cygnus A are: first, the high frequencies used; and second, the high sensitivity of the observations. The high frequencies enhance the probability to detect the flat spectrum free-free emission, against extended steep non thermal emission. The high frequencies also provide a higher angular resolution, which reduces the contamination from extended sources on larger scale. The high sensitivity is required given the expected low T_b of free-free emission. Specifically, in Cygnus A the possible free-free emission is at the 1 mJy level, compared to the total radio emission of ~ 100 Jy in this luminous nearby radio loud AGN.

4.5 Free-free emission from the Broad Line Region

The free-free emission likely detected in NGC 1068 (Section 4.2) and Cygnus A (Section 4.4) is produced at $r/r_{\text{dust}} \sim 600 - 1000$, which corresponds to the NLR scale. Free-free emission is also predicted to be produced by the photoionized gas in the BLR, but since free-free self-absorption is more prominent at the BLR, its detection requires observations above 100 GHz (see Fig. 3).

A unique signature of the free-free emission from photoionized gas in AGN is the expected spectral break between the NLR free-free emission and the BLR free-free emission. The break occurs due to the dust sublimation at r/r_{dust} of a few, and the consequent sharp rise in L_ν by a factor of ~ 10 around 100 GHz (Fig. 3). The detection of mm emission in RQ AGN is becoming feasible now with the ALMA array, which may already provide detections of the expected mm spectral break and the BLR free-free emission.

Figure 10 presents high frequency ALMA observations of NGC 1068 at 256 GHz (Impellizzeri et al. 2019), and 694 GHz (García-Burillo et al. 2016), which show a rising emission component with corresponding fluxes of 6.6 mJy and 13.8 mJy, implying a local spectral slope of $\alpha = 0.74$. This component resides significantly above an extrapolation of the VLBA low frequency PL component, which contributes at most about half the ALMA detected flux, when extrapolated to 256 GHz. The ALMA beam size used at 256 GHz is ~ 20 mas, and ~ 60 mas at 694 GHz (García-Burillo et al. 2016; Impellizzeri et al. 2019), which raises the possibility that the flux rise is a beam size effect for a diffuse source. However, the fluxes measured by Inoue et al. (2020) above 100 GHz, with a beam size of ~ 30 mas, lead to a similar spectral shape, which suggests the flux rise is real and not a beam size effect.

The steeply rising excess emission above 100 GHz is remarkably similar to the predicted free-free emission of RPC gas on the BLR scale, which is characterised by $\nu_{\text{thick}} > 100$ GHz (Fig. 3). The excess flux is well described by dustless RPC gas with $\Omega = 0.025$ located at $r/r_{\text{dust}} = 3.1$, assuming an underlying flat PL $\alpha = -0.17$ component, or $\Omega = 0.03$ and $r/r_{\text{dust}} = 4.2$ for an assumed steep PL component with $\alpha = -0.9$. For dusty gas free-free emission, the corresponding best fit parameters are $\Omega = 0.23$ and $r/r_{\text{dust}} = 1.1$ for $\alpha = -0.17$, and $\Omega = 0.28$ and $r/r_{\text{dust}} = 1.7$ for $\alpha = -0.9$. The smaller value of r for dusty gas is due to the lower τ of dusty RPC gas at a given r/r_{dust} , and the larger Ω is due to the weaker emission of dusty gas (Fig. 3). The dustless solution is favoured by the dust physics and by the GRAVITY observation of a compact dusty disc at the same location (Gravity Collaboration et al. 2020), as further discussed below.

Excess mm emission, above the cm PL extrapolation, is commonly observed in RQ AGN (Doi et al. 2005, 2011; Behar et al. 2015, 2018), and sometimes shows an inverted slope of a rising flux with frequency. For example, Inoue & Doi (2018) find a flux rise above 20 GHz in NGC 985, and above 50 GHz in IC 4329A. However, ALMA observations above 100 GHz show a spectral steepening to -0.37 in NGC 985, and to -0.51 in IC 4329A (Inoue & Doi 2018, tables 1 and 2), which clearly excludes free-free emission, and suggests the mm excess emission is produced by compact optically thick synchrotron emission.

4.6 $L_{[\text{O III}]}$ versus L_{radio} , predicted versus observed

The RPC effect of photoionized gas leads to a unique ionization and density structure of the gas at the NLR and the BLR (Stern et al. 2014a; Baskin et al. 2014a), and thus to a unique solution for the line and continuum emission for a given incident flux. One can therefore use the line luminosity to predict the expected free-free luminosity, and compare it to the observed relation. The free-free emission from the BLR is restricted to $\nu > 100$ GHz, which is not readily available yet for RQ AGN. At $\nu < 100$ GHz, the free-free emission originates from the NLR, and we therefore use below the narrow line luminosity, specifically the $[\text{O III}] \lambda 5007$ line, which is the strongest line from the NLR, to explore the free-free versus line luminosity relation.

Figure 12 compares the predicted and observed relation between

the [O III] $\lambda 5007$ emission line luminosity and L_ν at $\nu = 5, 45$ and $95 - 100$ GHz, in radio quiet AGN. The left panel presents $L_{5\text{GHz}}$ versus $L_{[\text{O III}]}$ for the RQ PG quasars. The radio luminosities are taken from [Kellermann et al. \(1989\)](#), and the [O III] $\lambda 5007$ emission line luminosities are taken from [Boroson & Green \(1992\)](#).¹ The predicted relation is derived from the RPC dusty gas calculations for $r/r_{\text{dust}} = 10^{3.5} - 10^5$ (e.g. $r = 0.6 - 20$ kpc for $L_{46} = 1$), the range of distances where most of the [O III] $\lambda 5007$ line emission is expected to be produced ([Stern et al. 2014a](#), fig. 6). We use the value of $L_{5\text{GHz}}$ emitted from the illuminated side of the slab; and the total $L_{[\text{O III}]}$, as calculated by Cloudy, which mostly comes from the illuminated side. The Cloudy results imply a relation of

$$\log \nu L_{5\text{GHz}} = \log L_{[\text{O III}]} - 4.51. \quad (22)$$

The observed $L_{5\text{GHz}}$ versus $L_{[\text{O III}]}$ distribution of the RQ PG quasars lies well above the predicted relation, with a median observed excess of $L_{5\text{GHz}}$ above the free-free value of about a factor of 20. The objects with the lowest $L_{5\text{GHz}}$, at a given $L_{[\text{O III}]}$, are still a factor of ~ 5 above the free-free relation. Indeed, the observed radio spectral slope is typically either significantly steeper or flatter than $\alpha = -0.1$ of optically thin free-free emission, suggesting synchrotron emission, which is either optically thin or optically thick ([Laor et al. 2019](#)).

However, the predicted $L_{5\text{GHz}}$ is not always hopelessly swamped by the non thermal radio emission, in particular in those objects at the lowest $L_{5\text{GHz}}$ for a given $L_{[\text{O III}]}$. Also, since the free-free spectral slope is flat, it is expected to become more dominant at higher frequencies, in particular in objects dominated by a steep synchrotron emission.

What is the observed relation with $L_{[\text{O III}]}$ at higher radio frequencies? Figure 12, middle panel, compares the observed and the predicted relation between $L_{[\text{O III}]}$ and $L_{45\text{GHz}}$, for a small subset of 15 RQ AGN, selected randomly from the PG quasar sample ([Baldi et al. 2021](#)). The predicted relation based on RPC is

$$\log \nu L_{45\text{GHz}} = \log L_{[\text{O III}]} - 3.67. \quad (23)$$

The observed distribution of $L_{45\text{GHz}}$ versus $L_{[\text{O III}]}$ lies above the predicted relation, as found above for $L_{5\text{GHz}}$ (Fig. 12, left panel). However, the median excess flux is only a factor of ~ 5 above the predicted free-free emission, in contrast with the median excess flux of ~ 20 found above at 5 GHz.

What is the observed relation at yet higher radio frequencies? Figure 12, right panel, presents the observed relation between the radio luminosity at $\nu \approx 100$ GHz and $L_{[\text{O III}]}$, for a hard X-ray selected sample of mostly lower luminosity nearby AGN, some of which are obscured. We adopt the measured flux at $\nu = 95$ GHz from [Behar et al. \(2015\)](#), and at $\nu = 100$ GHz from [Behar et al. \(2018\)](#). The corresponding values of $L_{[\text{O III}]}$ are from [Koss et al. \(2017\)](#).² We also adopt from [Koss et al. \(2017\)](#) the distance and z of the sample objects, and convert the measured radio fluxes to L_ν . The PL fit of the modelled free-free emission at $\nu = 100$ GHz yields

$$\log \nu L_{100\text{GHz}} = \log L_{[\text{O III}]} - 3.36. \quad (24)$$

The observed distribution again reside above the free-free prediction, as found at 5 and 45 GHz. Objects at $\log L_{[\text{O III}]} > 41$ reside within a factor of 3 – 10 above the predicted free-free emission, while objects

at $\log L_{[\text{O III}]} < 41$ have a significantly larger excess. This could be just a selection effect, as only the higher $L_{100\text{GHz}}$ AGN are detectable when the sample extends to the lowest $L_{[\text{O III}]}$. Since some of the objects are obscured AGN, their $L_{[\text{O III}]}$ may be offset to lower values, which will also increase the deviation from the free-free relation.

4.7 The free-free continuum versus the observed SED

Figure 13 compares the predicted free-free continuum from RPC gas at various distances, with the observed mean SED of RQ AGN, scaled for $L_{\text{bol}} = 10^{46}$ erg s⁻¹. The mean SED is calculated as follows. In the range of $\nu = 10^{12.5} - 10^{17}$ Hz, we use the mean SED from [Richards et al. \(2006\)](#). We extend the SED to $\nu > 10^{17}$ Hz assuming a constant νL_ν , and to the sub-mm regime using the relation $L_\nu \propto \nu^{3.5}$ ([Symeonidis et al. 2016](#)). For the radio range, we adopt a PL $L_\nu \propto \nu^{-0.5}$, and use the normalisation $\nu L_\nu(5 \text{ GHz})/\nu L_\nu(10^{17} \text{ Hz}) = 6.25 \times 10^{-5}$ ([Laor & Behar 2008](#)), which corresponds to a radio loudness parameter of $R = 0.6$. For the RPC models, we present the free-free emitted from the illuminated side for $\Omega = 0.3$.

The predicted free-free continuum of most models lie well below the observed SED at most frequencies. The free-free SED is potentially significant, or even dominant, only at $\nu \approx 100 - 300$ GHz, located at the presumed sharp spectral break between the extrapolation of the radio cm band emission to the mm regime, and the extrapolation of the cold dust FIR emission to the sub mm regime. The free-free continuum of dusty gas models becomes comparable to the estimated mean SED luminosity at ~ 500 GHz. The free-free emission of dustless gas is a factor of ~ 10 stronger than dusty gas, and may dominate the assumed SED above 100 GHz, if significant dustless gas can be found outside the BLR at $r/r_{\text{dust}} \sim 10$. Free-free emission from dustless gas inside the BLR ($r/r_{\text{dust}} < 1$) can also be detected, despite the dominance of the sub mm tail of the cold dust emission at $\nu > 500$ GHz, as the free-free source is far more compact ($\ll 1$ mas) than the cold dust (~ 1 arcsec). The difference in T_b is also dramatic. In both dusty and dustless RPC gas, we expect free-free emission with $T_b \sim 2 - 3 \times 10^4$ K (Fig. 5). The dust emission at $\nu > 500$ GHz comes from the coldest dust, where $T_e < 100$ K. Also, the dust optical depth is inevitably very low. For example, at 600 GHz we expect $\tau \sim 0.07$ even for a very high mean column of 10^{24} cm⁻² ([Laor & Draine 1993](#), fig. 6). Since $T_b = \tau T_e$ for $\tau < 1$, the T_b of dust emission will be smaller by a factor $> 10^3$ than the T_b of the BLR-scale free-free emission.

Fig. 13 also explores the predicted free-free emission of photoionized gas which extends down to $r/r_{\text{dust}} = 0.01$, well inwards of the standard BLR. As r/r_{dust} decreases the gas becomes optically thick at higher ν (Fig. 2). The peak free-free L_ν increases with decreasing r/r_{dust} (see also Fig. 3). The emission at $\nu \gtrsim 10^{16}$ Hz is roughly independent of r/r_{dust} (Fig. 13). This ν -range roughly corresponds to $T \approx h\nu/k \gtrsim 5 \times 10^5$ K, and corresponds to the free-free emission from the hottest, optically thin, surface layer where the RPC gas reaches the Compton temperature at all distances ([Stern et al. 2014a](#); [Baskin et al. 2014a](#)). The emission from this optically thin layer is $L_\nu \propto n^2 r^2 l$, which is roughly independent of r/r_{dust} for RPC gas. Gas located at $r/r_{\text{dust}} = 0.01$ reaches a maximal density of $n \sim 10^{15}$ cm⁻³ in an RPC slab ([Baskin et al. 2014a](#)), which is the high-density limit of the photoionization code Cloudy. Thus, we refrain from extending the calculation to a smaller value of r/r_{dust} . Since the typical $r_{\text{dust}} \sim 10^4 r_g$, where $r_g = GM_{\text{BH}}/c^2$ is the gravitational radius, a value of $r/r_{\text{dust}} < 0.01$ corresponds to $r < 100 r_g$ which corresponds to the inner parts of the accretion disc, and the assumption of a point source illumination breaks down.

¹ The luminosities are derived using: $H_0 = 67.7$ km s⁻¹ Mpc⁻¹, $\Omega_m = 0.31$ and $\Omega_\Lambda = 0.69$.

² The value of $L_{[\text{O III}]}$ for the object Ark 564 is adopted from [Crenshaw et al. \(2002\)](#), since it is not covered by [Koss et al. \(2017\)](#) (the value of the luminosity distance is adopted from [Behar et al. 2015](#)). NGC 5106 is excluded from the sample since it is radio loud.

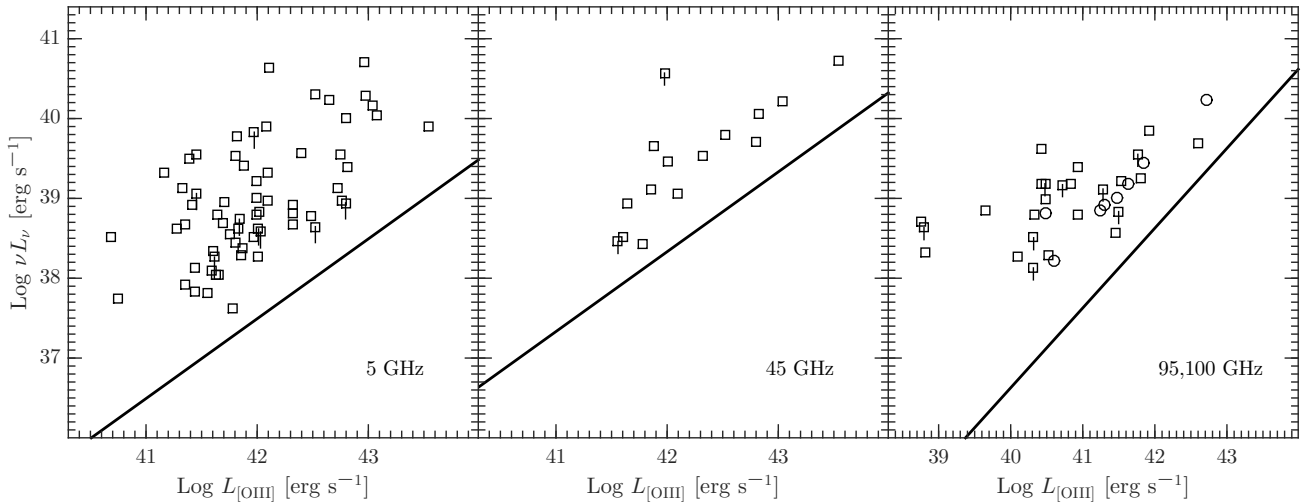


Figure 12. The predicted νL_ν versus $L_{[\text{O III}]}$ from Cloudy model results, compared to the observed distributions at $\nu = 5, 45$ and $95 - 100$ GHz. **Left panel:** The observed $L_{5\text{GHz}}$ versus $L_{[\text{O III}]}$ distribution for the radio quiet PG quasars (open squares), compared to the RPC based thermal free-free radio emission (solid line). The radio emission of all objects resides well above the predicted free-free $L_{5\text{GHz}}$, suggesting the radio is dominated by synchrotron emission, as also indicated by the observed range of spectral slopes. The objects with the lowest $L_{5\text{GHz}}$, at a given $L_{[\text{O III}]}$, are typically only a factor of ~ 5 above the predicted free-free emission. **Middle panel:** Same as the left panel for $L_{45\text{GHz}}$. The observed $L_{45\text{GHz}}$ of all objects is above the predicted free-free emission, but the median excess flux is now only a factor of ~ 5 , compared to a median excess of ~ 20 at 5 GHz (left panel). **Right panel:** Same as the left panel for $L_{95,100\text{GHz}}$. The objects are hard X-ray selected mostly nearby AGN, which are either obscured or unobscured. The observed distribution resides slightly closer to the predicted free-free emission. Note that some of these hard X-ray selected objects may be displaced due to $[\text{O III}]$ absorption.

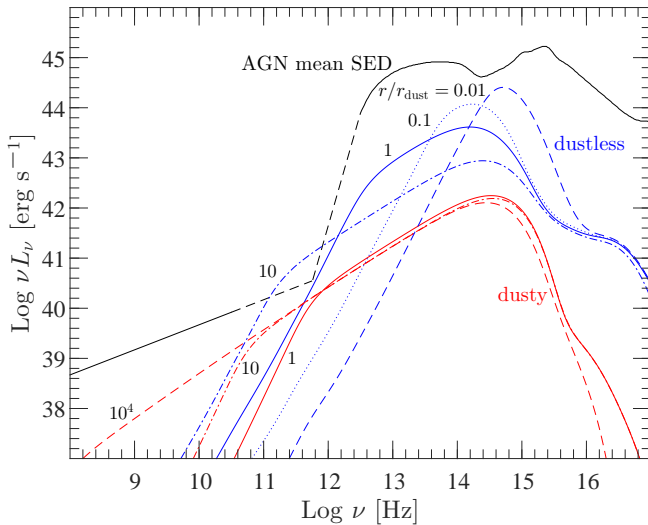


Figure 13. The RPC gas free-free continuum from gas located at various r/r_{dust} , compared to the mean observed AGN SED (black), scaled for $L_{\text{bol}} = 10^{46}$ erg s $^{-1}$. The RPC calculations are presented for dusty (red) and dustless (blue) gas. The free-free continuum of dustless gas which resides just outside the BLR ($r/r_{\text{dust}} \sim 10$) may be detectable at $\nu \approx 100 - 800$ GHz. Free-free emission at 1000 GHz (300 μm) may also be detectable, despite the dominant cold dust emission, as the dust emission is extended on arcsec (kpc) scale, compared to the micro arcsec (sub pc BLR) scale free-free emission.

5 DISCUSSION

5.1 Absorption

Radio absorption is a powerful tool for the detection of both neutral and ionized gas in AGN. Neutral gas can be probed through the H I 21 cm absorption line (e.g. Morganti et al. 2004), while ionized gas can be discovered through its free-free absorption (Sections 3.2

and 4.1). The great advantage of the radio is that it allows to spatially resolve the structure of the absorbing medium on mas, i.e. pc, scale. Such a spatial resolution of thermal emission and absorption is generally not achievable in other bands (with the exclusion of the recent outstanding GRAVITY results, e.g. Gravity Collaboration et al. 2020). The significant limitation of the radio method is that it requires a very bright radio background source on mas scale. So, this tool is restricted to the small subset of AGN which are both radio loud, and have a high T_b compact source. In addition, the spatial distribution of the absorbing medium is limited to gas which happened to reside in front of the radio source (e.g. Vermeulen et al. 1994; Ulvestad 1999; Gallimore et al. 1999; Walker et al. 2000; Jones et al. 2001; Kamenov et al. 2003).

The free-free absorbing gas on pc scale can be heated and ionized through various mechanisms. It can be viscous heating, if it resides within the accretion disc. It can be shock heating due to a wind or jet interaction with the ambient medium. It can be photoionized by the AGN, which is inevitable if the gas is exposed to the central source. In this case, the RPC effect is also inevitable, but it is not necessarily the dominant gas compression mechanism, as the gas may be magnetic pressure confined, or thermal pressure confined by a hot and dilute medium.

The unique advantage of the RPC solution is that it provides a unique prediction for τ_ν as a function of the distance of the absorbing gas from the ionizing source (Section 3.2). This is in contrast with non RPC photoionization solutions (e.g. Ulvestad et al. 1981; Krolik & Lepp 1989), where τ_ν depends on the unknown gas density. Thus, an observational determination of τ_ν does not yield the absorber distance. In contrast, the RPC effects produces such a relation. Specifically, absorbers on a scale of $r/r_{\text{dust}} \sim 1000$, or 10 to 100 pc for AGN at $L_{\text{bol}} \sim 10^{44}$ to 10^{46} erg s $^{-1}$, has $\nu_{\text{thick}} \sim 1$ GHz, and on scales of 1 – 10 pc will show $\nu_{\text{thick}} \sim 10$ GHz.

In the well studied case of NGC 1275 (Jones et al. 1996; Ulvestad et al. 1999; Peck et al. 1999; Vermeulen et al. 2003), we find that indeed the observed spatially resolved ν_{thick} matches the

RPC prediction, based on the luminosity of NGC 1275 and the spatially resolved physical distance of the absorber. Similar agreements are found for the spatially resolved free-free absorption in NGC 4151, NGC 4261, and in particular in NGC 1052 where ν_{thick} can be estimated at three positions which cover a factor of four in distance (Section 4.1).

One should note that there are no free parameters involved in the analysis of the objects above, as $\nu_{\text{thick}}(r)$ is uniquely set by L_{bol} and the absorber distance r , both directly observed (up to projection effect corrections, likely of order unity). The match of the predicted and observed $\nu_{\text{thick}}(r)$ indicates the following: 1. the absorbing gas is photoionized; and 2. the absorbing gas density is set by the incident radiation pressure, i.e. it is RPC gas.

The results above add to earlier evidence on that RPC sets the gas density in AGN. Specifically, the NLR density radial dependence and its ionization structure (Dopita et al. 2002; Stern et al. 2014a; Davies et al. 2016), the BLR emission radial dependence (Baskin et al. 2014a; Netzer 2020), the Broad Absorption Lines ionization structure (Baskin et al. 2014b; Mas-Ribas & Mauland 2019), the X-ray lines absorption measure distribution (Stern et al. 2014b), the X-ray lines emission measure distribution (Bianchi et al. 2019), and galactic scale winds (Stern et al. 2016; Mas-Ribas 2019; Somalwar et al. 2020). These results suggest that generally there is no additional significant confining mechanism for ionized gas in AGN, such as ambient magnetic or thermal pressure.

One can therefore use the detection of free-free absorption in the radio to derive the distance of the absorbing medium from the centre. This method should apply for gas on scales $\sim 0.1 - 100$ pc, where one expects $\nu_{\text{thick}} \sim 100 - 0.1$ GHz.

5.2 Emission

Detection of free-free emission in AGN at the cm regime (< 30 GHz) is challenging, as this regime is generally dominated by synchrotron emission. It is likely detected in Cygnus A (Carilli et al. 2019), and was suggested in NGC 1068 (Gallimore et al. 2004). Both sources are bright in the radio, though NGC 1068 is RQ, but is nearby and luminous. High S/N and high resolution imaging allows to detect the relatively faint free-free emission, which at the mJy flux level, close to the non thermal emission, which is a factor of $10^3 - 10^5$ brighter in the cm regime. Below we discuss several expected properties of the free-free emission and compare them to observations.

5.2.1 Predicted strength

What is the expected contribution of free-free emission to the observed radio emission in the cm range? The observed radio loudness parameter, $R = f_{\nu}(4400\text{\AA})/f_{\nu}(5\text{ GHz})$, is $R \sim 0.1 - 1$ for most RQ AGN (Kellermann et al. 1989). Adopting the mean AGN luminosity ratio $L_{\text{bol}}/\nu L_{\nu}(4400\text{\AA}) = 8$ (Richards et al. 2006), implies $L_{\nu}(4400\text{\AA}) = 1.8 \times 10^{-16} L_{\text{bol}}$. The RPC free-free solution yields a maximal contribution of $L_{\nu}^{\text{ff}}(5\text{ GHz}) = 5 \times 10^{-18} L_{\text{bol}}$ (Fig. 3). Thus, the radio loudness due to free-free emission is only $R^{\text{ff}}(5\text{ GHz}) = 0.028$. The typical cm radio emission observed in RQ AGN is clearly not produced by free-free emission. However, a fair fraction (~ 20 per cent) of RQ AGN have $R < 0.1$ (Kellermann et al. 1989, fig. 5), in particular the so-called radio silent AGN (e.g. Chiaraluce et al. 2019). In such objects, free-free emission can provide significant contribution, or possibly even dominate the cm radio emission.

The above $R^{\text{ff}}(5\text{ GHz})$ estimate assumes $\Omega = 0.3$ for the NLR

free-free emitting gas. A more accurate estimate of the expected NLR free-free emission can be derived from $L_{[\text{O III}]}$ (Fig. 12). The [O III] line is expected to be a particularly good predictor of the NLR free-free radio emission since the [O III] line is produced at $r/r_{\text{dust}} > 200$, where the gas densities, induced by RPC, are below the [O III] critical density (Stern et al. 2014a, fig. 6). This range overlaps well the range of r/r_{dust} where the 5 GHz free-free emission is produced (Fig. 3). A remaining free parameter, which can significantly affect the $L_{[\text{O III}]}$ versus $L_{5\text{ GHz}}^{\text{ff}}$ relation, is the gas metallicity, which affects the strength distribution among the different emission lines. The comparison with the [O III] observations, shows that indeed the observed radio emission is higher than predicted by at least a factor of $\sim 2 - 3$ or larger (Fig. 12).

The mean observed radio spectral slope at 5–8.5 GHz is $\alpha \sim -0.5$ (e.g. Laor et al. 2019), while free-free emission produces $\alpha \sim -0.1$. Thus, the relative contribution of the free-free emission is expected to increase at higher frequencies. Indeed, the detection of the free-free emission in Cygnus A is made at 18–48 GHz (Carilli et al. 2019). The free-free emission may dominate at $\nu > 100$ GHz, if it is produced by dustless gas just outside the BLR, for an underlying continuum with $\alpha \sim -0.5$, and radio loudness of $R = 0.6$ (Fig. 13). The free-free emission could be detectable at $\nu < 100$ GHz in objects with a steeper α and a lower R value.

5.2.2 Synchrotron or free-free mm emission?

Radio observations of RQ AGN at ~ 100 GHz typically show excess emission, compared to the low frequency extrapolation (Doi et al. 2005, 2011; Behar et al. 2015, 2018). In addition to free-free, an alternative mechanism which may produce the observed excess emission, is a compact optically thick synchrotron source. The observed spectrum will show a transition from optically thin steep PL synchrotron emission, to a flat PL optically thick emission. Such a transition is indeed expected if the compact synchrotron source is produced by a magnetized accretion disc corona (Field & Rogers 1993; Laor & Behar 2008; Inoue & Doi 2014; Rąginski & Laor 2016). Indeed, in NGC 1068 the excess emission observed by ALMA above 100 GHz, which is interpreted here as free-free emission from the BLR scale, may instead be produced by optically thick synchrotron emission (Inoue et al. 2020).

How can one determine if the excess high frequency emission is synchrotron or free-free emission? The simplest diagnostic is the value of α . If $\alpha < -0.1$, as found by Inoue & Doi (2018) in NGC 985 and IC 4329A at 100–200 GHz, then the free-free interpretation is clearly ruled out. In contrast, a slope of $\alpha > -0.1$ can be produced by both optically thick synchrotron and by optically thick free-free emission.

The other major difference between free-free and optically thick synchrotron emission is the physical scale of the emitting region. Significant free-free emission at ~ 100 GHz is produced at $r/r_{\text{dust}} > 10$ (Fig. 3), while the corresponding scale for optically thick synchrotron emission is $r < 300r_{\text{g}}$ (Rąginski & Laor 2016, fig. 4), which roughly corresponds to $r/r_{\text{dust}} < 0.03$. A flat spectrum synchrotron source is therefore expected to be more compact than a flat spectrum free-free source by a factor of > 300 .

5.2.3 Resolving the free-free emission region

What is the expected angular scale of the BLR scale free-free emission? In a nearby AGN, say at 100 Mpc, with moderate luminosity, say $L_{\text{bol}} = 10^{44}$ erg s^{-1} , where $r_{\text{dust}} = 0.02$ pc (eq. 11), the corresponding angular scales are > 0.4 mas for free-free emission, and

$< 1.3 \mu\text{as}$ for optically thick synchrotron emission. These angular scales are well below the maximal resolution of the ALMA array. The angular resolution is $\Theta = \lambda/D$, and for the ALMA array baseline of $D = 16 \text{ km}$, and for observations at 100 GHz, the angular resolution is only $\Theta = 0.3/1.6 \times 10^6 = 1.9 \times 10^{-7} = 38 \text{ mas}$.

Can the emission be resolved using the Event Horizon Telescope (EHT)? The EHT is working at $\lambda = 0.13 \text{ cm}$, with $D \approx 10,000 \text{ km}$, and thus reaches $\Theta_{\text{EHT}} = 25 \mu\text{as}$, and can resolve well the free-free emission scale. Indeed, the EHT resolves the emission down to $\sim 10r_g$ in M 87 (Event Horizon Telescope Collaboration et al. 2019). However, the expected enclosed flux within an angular scale of $\Theta = \Theta_{\text{mas}} \text{ mas}$, of a source with $T_b = 10^9 T_9 \text{ K}$, at $\nu = 10^{11} \nu_{100} \text{ GHz}$ Hz is

$$F_\nu = \Theta^2 \frac{2\nu^2}{c^2} k T_b = 7.2 \times 10^{-23} \Theta_{\text{mas}}^2 T_9 \nu_{100}^2 \text{ erg s}^{-1} \text{ Hz}^{-1} \text{ cm}^{-2} \quad (25)$$

(e.g. Rybicki & Lightman 2004), or

$$F_\nu = 7.2 \Theta_{\text{mas}}^2 \nu_{100}^2 T_9 \text{ Jy}. \quad (26)$$

Thus, a synchrotron source, with say $T_b \sim 10^{11} \text{ K}$, as expected for equipartition between the B field and the electron energy densities (Readhead 1994), will produce a flux of $F_\nu \sim 0.5 \text{ Jy}$ on the Θ_{EHT} resolution scale. This is indeed the flux observed in M87 by the Event Horizon Telescope Collaboration et al. (2019). However, in RQ AGN, where $\Theta < 1.2 \mu\text{as}$ (see above) a value of $T_b \sim 10^{11} \text{ K}$ gives $F_\nu \sim 10 \mu\text{Jy}$. So, the synchrotron source will be detectable only if T_b is well above 10^{11} K . Free-free emission at 100 GHz, from $r/r_{\text{dust}} > 10$, is characterised by $T_b < 1.5 \times 10^4 \text{ K}$ (Fig. 5), which corresponds to a tiny flux of $F_\nu \sim 0.1 \mu\text{Jy}$ (eq. 26), which is far too weak to be detectable by the EHT.

Thus, only the more extended NLR-scale free-free emission can be detected and resolved, assuming the specific array used has a low enough T_b detection limit, which allows to detect optically thin free-free emission.

5.2.4 Variability

An indirect but robust upper limit on the size of the emitting region is variability. In a typical luminous Seyfert ($L_{\text{bol}} = 10^{44} \text{ erg s}^{-1}$), the 100 GHz free-free emitting region is at $10r_{\text{dust}} \sim 0.2 \text{ pc}$, so can vary only on a year time scale. A synchrotron source originates from a region ~ 300 times smaller, and can therefore vary on a single day time scale.

Recurrent 100 GHz observations of a few nearby low luminosity AGN by Doi et al. (2011) suggest possible variability on time scales as short as days. The only long term mm monitoring campaign of a RQ AGN is available for NGC 7469 (Baldi et al. 2015; Behar et al. 2020), which indicates significant variability on a time scale of a couple of days. The host subtracted optical continuum luminosity of NGC 7469 is $2 \times 10^{43} \text{ erg s}^{-1}$ (Bentz et al. 2009), which indicates $L_{\text{bol}} \approx 2 \times 10^{44} \text{ erg s}^{-1}$. The observed 100 GHz variability on time scale of a couple of days clearly excludes free-free emission, which can vary only on year time scale for this L_{bol} , but is consistent with the expected size of an optically thick synchrotron source. Thus, although the spectral slope at $\sim 100 - 300 \text{ GHz}$ is $\alpha \approx 0$ (Behar et al. 2020, fig. 2), which is consistent with free-free emission, the emitting region is far too compact. A similar conclusion is reached based on the observed $L_{100 \text{ GHz}}/L_{\text{bol}} = 3 \times 10^{-16} \text{ Hz}^{-1}$, which is a factor ~ 10 larger than expected for free-free emission from optically thin dustless gas (Fig. 3), and must therefore be dominated by synchrotron emission. The observed high $L_{100 \text{ GHz}}/L_{[\text{O III}]}$ luminosity ratio also leads to a similar conclusion.

5.2.5 Dilution by dust emission

How high in frequency can we probe the free-free emission? The advantage of going to higher frequencies is that the free-free flux density either rises steeply (optically thick), or remains nearly constant (optically thin). The free-free flux drop occurs only in the optical regime or above (Fig. 13). In contrast, the synchrotron emission drops once the emission becomes optically thin, which is expected to occur below 1000 GHz in RQ AGN (Raginski & Laor 2016). Thus, the free-free emission is more likely to become dominant only at the sub mm regime ($> 300 \text{ GHz}$). However, the observed mean radio and FIR SED extrapolated to the sub mm regime, suggests that the steeply rising dust emission dominates above $\sim 500 \text{ GHz}$ (Fig. 13). The FIR extrapolation of the AGN contribution is subject to significant uncertainty (e.g. Bernhard et al. 2021), which adds to the uncertain host contribution. Despite this somewhat uncertain sharply rising ‘‘dust wall’’ at $\nu > 500 \text{ GHz}$ ($\propto \nu^{3.5}$), it may be possible to identify the nuclear free-free and synchrotron emission. The cold dust emission extends on the host galaxy scale, i.e. on arcsec scale, which will be resolved out using sub mm interferometry, in particular with ALMA. For example, Garca-Burillo et al. (2016) detect a $\sim 10 \text{ mJy}$ source on a scale of $\sim 50 \text{ mas}$ in the core of NGC 1068 at $\sim 430 \mu\text{m}$, while the total flux measured at $\sim 400 \mu\text{m}$ in NGC 1068, on a scale of 75 arcsec , is $\sim 30 \text{ Jy}$ (Hildebrand et al. 1977), i.e. a factor of 3000 brighter. Thus, the highest frequency where nuclear scale free-free emission can be probed, depends on the highest frequency currently available on sub mm interferometry (currently 950 GHz on ALMA).

5.2.6 NGC 1068

Above we showed (Section 4.2) that the observed flat, $\alpha_{5-8.4 \text{ GHz}} = -0.17 \pm 0.24$, compact VLBA scale radio emission cannot be produced by free-free emission, for the following reasons. First, the observed T_b is too high compared to the expected value for photoionized gas, of either RPC or uniform density gas. Second, this source lies behind a free-free absorbing screen, and the absorption corrected slope is too steep to agree with free-free emission.

We then find that the free-free emission of the absorbing screen, which resides at the NLR scale ($r/r_{\text{dust}} \approx 1000$), is consistent with the observed diffuse emission on the same scale, both in amplitude and spectral slope. One should note, however, that separating out the true diffuse emission from the compact synchrotron sources, is subject to some uncertainty. Thus, the detection of the free-free emission from the NLR-scale free-free absorbing screen is only tentative.

A potentially more exciting result is the possible detection of free-free emission from photoionized gas on the BLR scale, which can produce the excess emission observed by ALMA above 100 GHz (Section 4.5). The implied physical scale, based on the RPC results for dustless gas, is $r/r_{\text{dust}} = 3 - 4$, with a small covering factor of $\Omega = 0.025 - 0.03$. Dusty gas, subject to RPC, gives a smaller region $r/r_{\text{dust}} = 1.1 - 1.7$ with a larger $\Omega = 0.23 - 0.28$. Since $r_{\text{dust}} = 0.04 - 0.14 \text{ pc}$ (Section 4.2), the absolute size of the free-free emitting region is $r = 0.12 - 0.56 \text{ pc}$ for dustless gas, and $r = 0.044 - 0.24 \text{ pc}$ for dusty gas.

The recent *K*-band interferometry of NGC 1068 with GRAVITY (Gravity Collaboration et al. 2020), reveals a flat ring-like structure, with a radius $r = 0.24 \pm 0.03 \text{ pc}$, and a scale height $h/r < 0.14$. The RPC results for dustless gas, $r = 0.34 \pm 0.24 \text{ pc}$, $h/r = 0.14 \pm 0.1$ is consistent with the GRAVITY results, both in size and covering factor.

The NIR SED in NGC 1068, and generally in AGN, clearly shows that the *K*-band emission is produced by hot dust. Why do the RPC

results suggest that the photoionized free-free emitting gas is dustless? A likely explanation is the nature of the dust. As pointed out in [Baskin & Laor \(2018\)](#), only large graphite grains survive the direct illumination of the AGN at $r/r_{\text{dust}} \sim 1$. The UV absorption cross sections of dusty gas composed of large grains is significantly reduced ([Baskin & Laor 2018](#), fig. 7), so the depth of the photoionized layer and the associated free-free emission, remain similar to that of dustless gas. The large dust grains are heated by the UV (although they do not dominate the UV opacity) and cool by NIR emission, producing the K -band emission.

An alternative interpretation of the excess mm emission above 100 GHz in NGC 1068 is the contribution of an optically thick synchrotron emission ([Inoue et al. 2020](#)), which resides on the innermost accretion disc scales ([Raginski & Laor 2016](#)), and is likely produced within the accretion disc corona ([Field & Rogers 1993](#); [Laor & Behar 2008](#)). The implied size is \sim a light day, compared to \sim a light year for the free-free emission. In addition, one expects some relation between the mm synchrotron emission and the X-ray emission, as both can be produced in the same region. Thus, variability studies can exclude the free-free origin of the mm excess in NGC 1068.

The advantage of the BLR free-free interpretation, is that it naturally produces a spectral turnover at ν just below ~ 1000 GHz, as observed in NGC 1068; in contrast with the synchrotron interpretation, where the turnover depends on the outer radius of the magnetised plasma cloud, and there is no obvious preference for a specific radius.

In principle, interferometry at $\nu > 1000$ GHz can determine if the emission slope remains flat, as expected for optically thin free-free emission, or becomes steep since a synchrotron source is expected to become optically thin ([Raginski & Laor 2016](#)). However, a THz interferometry is not yet available, so this test cannot be made.

6 CONCLUSIONS

Ionizing radiation likely sets the ionization, temperature and density structure of the gas it is incident upon, and therefore the line and continuum emission of the gas. Following earlier studies in this series, on the emission and absorption properties of radiation pressure compressed photoionized gas, here we focus on the radio regime, in particular the free-free emission and absorption of RPC gas in AGN. We find the following:

(i) The distance of a free-free absorbing gas screen from an ionizing source of a given luminosity, can be found based on the frequency where the absorber becomes optically thick. The validity of the distance derived with this method is verified in a few objects where the free-free absorber is spatially resolved.

(ii) Free-free emission from gas at the NLR, at the kpc scale, is self-absorbed below a few hundred MHz. On the hundred pc scale, self-absorption sets in below a few GHz, and at the BLR scale free-free self-absorption sets in below a few hundred GHz.

(iii) The peak of the free-free emission, which occurs slightly above the self-absorption frequency, is characterised by $T_b < 2 \times 10^4$ K for free-free emission at all distances.

(iv) Radio emission with $T_b > 10^6$ K, as observed in NGC 1068, cannot be produced by free-free emission from hot gas, as the free-free emission of such hot gas over predicts the observed X-ray emission.

(v) Free-free emission produces a radio loudness parameter of $R^{\text{ff}}(5 \text{ GHz}) \sim 0.03$, while the typical observed value is $R \sim 0.1 - 1$. Thus, free-free emission may be significant at 5 GHz only in RQ AGN where $R < 0.1$.

(vi) The typical contribution of free-free emission in the radio is expected to rise with frequency, and may dominate at $\nu > 100$ GHz in some RQ AGN. In particular, if the free-free emission originates in dustless gas just outside the BLR.

(vii) The excess mm emission observed in NGC 1068 above 100 GHz, may be produced by photoionized gas at a distance of $r = 0.12 - 0.56$ pc. This size matches the size of hot dust ring, spatially resolved by GRAVITY, at $r = 0.24$ pc.

(viii) Excess mm emission above 100 GHz can also be produced by a compact synchrotron source at the innermost accretion disc. It differs dramatically in size from a free-free source, being ~ 300 times smaller, and can therefore be differentiated based on the variability time scale.

(ix) Optimal detection of free-free emission is through mm and sub mm interferometry, using an array which can detect emission at $T_b < 10^4$ K, such as ALMA. Such observations can map the spatial distribution of warm photoionized gas in AGN on the sub pc scale, even if this region is highly absorbed in the optical and in the X-ray regimes.

The improved sensitivity of sub mm interferometers now allows to study RQ AGN. Apart from studies of molecular gas emission lines, such observations can also probe the presence of warm photoionized gas on the sub pc scale, and potentially also detect non thermal emission from the innermost accretion disc scale ([Panessa et al. 2019](#)).

ACKNOWLEDGEMENTS

We thank the referee, G. Bicknell, for a thorough and careful review which improved the paper. AB thanks the hospitality of the Physics Department, Technion – Israel Institute of Technology, where this work had been conceived during his stay as a post-doctoral fellow in 2016. This research was supported by the Israel Science Foundation (grant no. 1008/18).

DATA AVAILABILITY

The data underlying this article will be shared on reasonable request to the corresponding author.

REFERENCES

- Antonucci R., Barvainis R., 1988, *ApJL*, 332, L13
 Baldi R. D., Behar E., Laor A., Horesh A., 2015, *MNRAS*, 454, 4277
 Baldi R. D., Laor A., Behar E., Horesh A., Panessa F., McHardy I., Kimball A., 2021, arXiv, arXiv:2107.14490
 Baldwin J., Ferland G., Korista K., Verner D., 1995, *ApJL*, 455, L119
 Baskin A., Laor A., Stern J., 2014a, *MNRAS*, 438, 604
 Baskin A., Laor A., Stern J., 2014b, *MNRAS*, 445, 3025
 Baskin A., Laor A., 2018, *MNRAS*, 474, 1970
 Barvainis R., Lonsdale C., Antonucci R., 1996, *AJ*, 111, 1431
 Behar E., Baldi R. D., Laor A., Horesh A., Stevens J., Tzioumis T., 2015, *MNRAS*, 451, 517
 Behar E., Vogel S., Baldi R. D., Smith K. L., Mushotzky R. F., 2018, *MNRAS*, 478, 399
 Behar E., Kaspi S., Paubert G., Billot N., Peretz U., Baldi R. D., Laor A., et al., 2020, *MNRAS*, 491, 3523
 Bentz M. C., Peterson B. M., Netzer H., Pogge R. W., Vestergaard M., 2009, *ApJ*, 697, 160
 Bernhardt E., Tadhunter C., Mullaney J. R., Grimmer L. P., Rosario D. J., Alexander D. M., 2021, *MNRAS*, 503, 2598. doi:10.1093/mnras/stab419

- Bianchi S., Guainazzi M., Laor A., Stern J., Behar E., 2019, *MNRAS*, 485, 416
- Binette L., 1998, *MNRAS*, 294, L49
- Boroson T. A., Green R. F., 1992, *ApJS*, 80, 109
- Callingham J. R. et al., 2017, *ApJ*, 836, 174. doi:10.3847/1538-4357/836/2/174
- Carilli C. L., Perley R. A., Dhawan V., Perley D. A., 2019, *ApJL*, 874, L32
- Chiara-luce E. et al., 2019, *MNRAS*, 485, 3185
- Crenshaw D. M., et al., 2002, *ApJ*, 566, 187
- Cusumano G. et al., 2010, *A&A*, 524, A64. doi:10.1051/0004-6361/201015249
- Davies R. L. et al., 2016, *ApJ*, 824, 50
- Doi A., Kameno S., Kohno K., Nakanishi K., Inoue M., 2005, *MNRAS*, 363, 692
- Doi A., Nakanishi K., Nagai H., Kohno K., Kameno S., 2011, *AJ*, 142, 167
- Dopita M. A., Groves B. A., Sutherland R. S., Binette L., Cecil G., 2002, *ApJ*, 572, 753
- Draine B. T., 2011a, *Physics of the Interstellar and Intergalactic Medium*. Princeton Univ. Press, Princeton, NJ
- Draine B. T., 2011b, *ApJ*, 732, 100
- Eddington A. S., 1916, *MNRAS*, 77, 16
- Event Horizon Telescope Collaboration, Akiyama K. et al., 2019, *ApJL*, 875, L1
- Eracleous M., Hwang J. A., Flohic H. M. L. G., 2010, *ApJS*, 187, 135
- Ferland G. J. et al., 2013, *RMxAA*, 49, 137
- Ferland G. J. et al., 2017, *RMxAA*, 53, 385
- Field G. B., Rogers R. D., 1993, *ApJ*, 403, 94
- Fujita Y., Nagai H., 2017, *MNRAS*, 465, L94
- Gallimore J. F., Baum S. A., O'Dea C. P., Pedlar A., 1996, *ApJ*, 458, 136
- Gallimore J. F., Baum S. A., O'Dea C. P., 1997, *Nature*, 388, 852
- Gallimore J. F., Baum S. A., O'Dea C. P., Pedlar A., Brinks E., 1999, *ApJ*, 524, 684
- Gallimore J. F., Baum S. A., O'Dea C. P., 2004, *ApJ*, 613, 794
- García-Burillo S. et al., 2016, *ApJL*, 823, L12
- García-Burillo S. et al., 2019, *A&A*, 632, A61
- Giroletti M., Panessa F., 2009, *ApJL*, 706, L260
- Gopal-Krishna et al., 2014, *MNRAS*, 443, 2824. doi:10.1093/mnras/stu1364
- Gravity Collaboration et al., 2020, *A&A*, 634, A1
- Groves B. A., Dopita M. A., Sutherland R. S., 2004, *ApJS*, 153, 9
- Hildebrand R. H., Whitcomb S. E., Winston R., Stiening R. F., Harper D. A., Moseley S. H., 1977, *ApJ*, 216, 698
- Inoue Y., Doi A., 2014, *PASJ*, 66, L8
- Inoue Y., Doi A., 2018, *ApJ*, 869, 114
- Inoue Y., Khangulyan D., Doi A., 2020, *ApJL*, 891, L33
- Impellizzeri C. M. V. et al., 2019, *ApJL*, 884, L28
- Jones D. L. et al., 1996, *ApJL*, 466, L63
- Jones D. L., Wehrle A. E., Piner B. G., Meier D. L., 2001, *ApJ*, 553, 968
- Kameno S., Inoue M., Wajima K., Sawada-Satoh S., Shen Z.-Q., 2003, *PASA*, 20, 134. doi:10.1071/AS03003
- Kellermann K. I., Sramek R., Schmidt M., Shaffer D. B., Green R., 1989, *AJ*, 98, 1195
- Krolik J. H., Lepp S., 1989, *ApJ*, 347, 179
- Koss M. et al., 2017, *ApJ*, 850, 74
- Laor A., Behar E., 2008, *MNRAS*, 390, 847
- Laor A., Draine B. T., 1993, *ApJ*, 402, 441
- Laor A., Baldi R. D., Behar E., 2019, *MNRAS*, 482, 5513
- Levinson A., Laor A., Vermeulen R. C., 1995, *ApJ*, 448, 589
- Marr J. M., Taylor G. B., Crawford F., 2001, *ApJ*, 550, 160. doi:10.1086/319729
- Mas-Ribas L., 2019, *ApJ*, 885, 95
- Mas-Ribas L., Mauland R., 2019, *ApJ*, 886, 151
- Menzel D. H., 1968, *Nature*, 218, 756
- Middelberg E. et al., 2004, *A&A*, 417, 925
- Mhaskey M., Gopal-Krishna, Dabhade P., Paul S., Salunkhe S., Sirothia S. K., 2019, *MNRAS*, 485, 2447. doi:10.1093/mnras/stz335
- Morganti R., Greenhill L. J., Peck A. B., Jones D. L., Henkel C., 2004, *NewAR*, 48, 1195
- Mundell C. G., Wilson A. S., Ulvestad J. S., Roy A. L., 2000, *ApJ*, 529, 816
- Murray N., Quataert E., Thompson T. A., 2010, *ApJ*, 709, 191
- Netzer H., 2020, *MNRAS*, 494, 1611
- O'Dea C. P., Saikia D. J., 2021, *A&ARv*, 29, 3. doi:10.1007/s00159-021-00131-w
- Ogle P. M., Brookings T., Canizares C. R., Lee J. C., Marshall H. L., 2003, *A&A*, 402, 849
- Onken C. A. et al., 2007, *ApJ*, 670, 105
- Osterbrock D. E., Ferland G. J., 2006, *Astrophysics of Gaseous Nubulae and Active Galactic Nuclei*, 2nd ed.. Univ. Science Books, Sausalito, CA
- Panessa F., Baldi R. D., Laor A., Padovani P., Behar E., McHardy I., 2019, *NatAs*, 3, 387
- Peck A. B., Taylor G. B., Conway J. E., 1999, *ApJ*, 521, 103
- Pedlar A., Fernandez B., Hamilton N. G., Redman M. P., Dewdney P. E., 1998, *MNRAS*, 300, 1071
- Pier E. A., Voit G. M., 1995, *ApJ*, 450, 628
- Raginski I., Laor A., 2016, *MNRAS*, 459, 2082
- Readhead A. C. S., 1994, *ApJ*, 426, 51
- Richards G. T. et al., 2006, *ApJS*, 166, 470
- Roy A. L., Colbert E. J. M., Wilson A. S., Ulvestad J. S., 1998, *ApJ*, 504, 147
- Rybicki G. B., Lightman A. P., 2004, *Radiative Processes in Astrophysics*. WILEY-VCH Verlag GmbH & Co. KGaA, Weinheim, Germany
- Somalwar J. et al., 2020, *ApJL*, 890, L28
- Stern J., Laor A., Baskin A., 2014, *MNRAS*, 438, 901
- Stern J., Behar E., Laor A., Baskin A., Holczer T., 2014, *MNRAS*, 445, 3011
- Stern J., Faucher-Giguère C.-A., Zakamska N. L., Hennawi J. F., 2016, *ApJ*, 819, 130
- Storey P. J., Hummer D. G., 1995, *MNRAS*, 272, 41
- Symeonidis M., Giblin B. M., Page M. J., Pearson C., Bendo G., Seymour N., Oliver S. J., 2016, *MNRAS*, 459, 257
- Tadhunter C., Marconi A., Axon D., Wills K., Robinson T. G., Jackson N., 2003, *MNRAS*, 342, 861
- Thompson T. A., Quataert E., Murray N., 2005, *ApJ*, 630, 167
- Ulvestad J. S., 1999, *AdSpR*, 23, 1029
- Ulvestad J. S., Ho L. C., 2001, *ApJL*, 562, L133
- Ulvestad J. S., Wilson A. S., Sramek R. A., 1981, *ApJ*, 247, 419
- Ulvestad J. S., Wrobel J. M., Carilli C. L., 1999, *ApJ*, 516, 127
- Vermeulen R. C., Readhead A. C. S., Backer D. C., 1994, *ApJL*, 430, L41
- Vermeulen R. C., Ros E., Kellermann K. I., Cohen M. H., Zensus J. A., van Langevelde H. J., 2003, *A&A*, 401, 113
- Walker R. C., Romney J. D., Benson J. M., 1994, *ApJL*, 430, L45
- Walker R. C., Dhawan V., Romney J. D., Kellermann K. I., Vermeulen R. C., 2000, *ApJ*, 530, 233
- Xu C., Livio M., Baum S., 1999, *AJ*, 118, 1169

This paper has been typeset from a $\text{\TeX}/\text{\LaTeX}$ file prepared by the author.